

Creating and using large grids of precalculated model atmospheres for a rapid analysis of stellar spectra

J. Zsargó^{1,2}, C. R. Fierro-Santillán³, J. Klapp^{1,3} e-mail: jaime.klapp@inin.gob.mx, A. Arrieta⁴, L. Arias⁴, J. M. Valencia², L. Di G. Sigalotti⁵, M. Hareter⁵, and R. E. Puebla^{6,7}

¹ Environmental Physics Laboratory (EPHYSLAB), Facultad de Ciencias, Campus de Ourense, Universidad de Vigo, Ourense 32004, Spain

² Departamento de Física, Escuela Superior de Física y Matemáticas, Instituto Politécnico Nacional, Avenida Instituto Politécnico Nacional S/N, Edificio 9, Gustavo A. Madero, San Pedro Zacatenco, 07738 Ciudad de México, Mexico

³ Departamento de Física, Instituto Nacional de Investigaciones Nucleares (ININ), Carretera México-Toluca km. 36.5, La Marquesa, 52750 Ocoyoacac, Estado de México, Mexico,

⁴ Universidad Iberoamericana, Prolongación Paseo de la Reforma 880, Alvaro Obregon, Lomas de Santa Fe, 01219 Ciudad de México, Mexico,

⁵ Departamento de Ciencias Básicas, Universidad Autónoma Metropolitana-Azcapotzalco (UAM-A), Av. San Pablo 180, 02200 Ciudad de México, Mexico

⁶ Facultad de Ingeniería, Ciencias Físicas y Matemática, Universidad Central del Ecuador, Ciudadela Universitaria, Quito, Ecuador

⁷ Centro de Física, Universidad Central del Ecuador, Ciudadela Universitaria, Quito, Ecuador

Received MM DD, 2020; Accepted MM DD, 2020

ABSTRACT

Aims. We present a database of 43,340 atmospheric models (~80,000 models at the conclusion of the project) for stars with stellar masses between 9 and 120 M_{\odot} , covering the region of the OB main-sequence and Wolf-Rayet (W-R) stars in the Hertzsprung–Russell (H–R) diagram.

Methods. The models were calculated using the ABACUS I supercomputer and the stellar atmosphere code CMFGEN.

Results. The parameter space has six dimensions: the effective temperature T_{eff} , the luminosity L , the metallicity Z , and three stellar wind parameters: the exponent β , the terminal velocity V_{∞} , and the volume filling factor F_{cl} . For each model, we also calculate synthetic spectra in the UV (900–2000 Å), optical (3500–7000 Å), and near-IR (10000–40000 Å) regions. To facilitate comparison with observations, the synthetic spectra can be rotationally broadened using ROTIN3, by covering $v \sin i$ velocities between 10 and 350 km s⁻¹ with steps of 10 km s⁻¹.

Conclusions. We also present the results of the reanalysis of ϵ Ori using our grid to demonstrate the benefits of databases of precalculated models. Our analysis succeeded in reproducing the best-fit parameter ranges of the original study, although our results favor the higher end of the mass-loss range and a lower level of clumping. Our results indirectly suggest that the resonance lines in the UV range are strongly affected by the velocity-space porosity, as has been suggested by recent theoretical calculations and numerical simulations.

Key words. astronomical databases: miscellaneous — methods: data analysis — stars: atmospheres

1. Introduction

The self-consistent analysis of spectral regions from the X-ray to the IR is now possible because of the fertile combination of the large amount of observational data and the availability of sophisticated stellar atmosphere codes, such as CMFGEN (Hillier 2013; Hillier & Miller 1998, 1999; Puebla et al. 2016), PHOENIX (Hauschildt 1992), TLUSTY (Hubeny & Lanz 1995), WM-BASIC (Pauldrach et al. 2001), FASTWIND (Santolaya-Rey et al. 1997; Puls et al. 2005; Rivero González et al. 2011; Carneiro et al. 2016), and the Potsdam Wolf-Rayet (W-R) code (PoWR, Gräfener et al. 2002; Hamann & Gräfener 2004; Sander et al. 2015). As a result, significant advances have been made in our understanding of the physical conditions in the atmospheres and winds of massive stars. In parallel with these advances, stellar atmosphere codes were also improved and became even more sophisticated.

For example, early far-UV observations (Fullerton et al. 2000) showed inconsistencies between the optical effective tem-

perature scale and the temperature that was implied by the observed wind ionization. Studies by Martins et al. (2002) and others showed that the neglect of line blanketing in the atmospheric models resulted in a systematic overestimate of the effective temperature derived from optical H and He lines. After these effects were introduced into the stellar atmosphere models, the inconsistencies were eliminated. Studies by Crowther et al. (2002), Hillier et al. (2003), and Bouret et al. (2003), who simultaneously analyzed *FUSE*, *HST*, and optical spectra of O stars with the corrected models, were able to derive consistent effective temperatures using a wide variety of diagnostics.

Another crucial development was the recognition of the important effects of the line-deshadowing instabilities (LDI or clumping) on the spectral analyses of O, B, and W-R stars. For example, Crowther et al. (2002) and Hillier et al. (2003) were unable to reproduce the observed P V $\lambda\lambda 1118$ – 1128 profiles when they used mass-loss rates derived from the analysis of H α . The only way in which the P V and H α profile discrepancies

could be resolved were either to assume substantial clumping or to use unrealistically low phosphorus abundances. As a consequence of the introduction of clumping, the mass-loss rates were lowered by significant factors (from 3 to 10). The analysis of the high-resolution X-ray observations of the *Chandra* and *XMM-Newton* X-ray observatories provided further support to the idea of a reduced mass-loss rate. The strong emission lines produced by H and He-like ions of O, Ne, Mg, and Si are far less strongly absorbed by the cold wind than previously expected (e.g., Cassinelli et al. 2001; Kahn et al. 2001). For example, Cohen et al. (2006, 2010), Cohen et al. (2014), and Gagné et al. (2005) analyzed the bound-free absorption by the wind in massive stars observed by *Chandra* and found mass-loss rates that were up to ten times lower than previous estimates.

Including X-ray regions into self-consistent stellar atmospheric models also resulted in the introduction of the non-vacuum interclump medium in the wind models. The only way Zsargó et al. (2008) were able to reproduce the strong O VI and N V lines in the far-UV (FUV) spectra of ζ Pup were to abandon the assumption of vacuum between clumps. Now, we know that these super-ions are primarily produced by Auger ionization by X-rays in the rarified interclump medium (see also Puebla et al. 2016). Furthermore, ideas to explain the low wind absorption on the X-ray emission lines by Oskinova et al. (2004) that invoked optically thick clumping, although they were refuted by Owocki & Cohen (2006) and Sundqvist et al. (2012), led to the recognition of the importance of velocity-space porosity (vorosity) effects on strong UV lines (Sundqvist et al. 2014; Sundqvist & Puls 2018, and references therein).

Unfortunately, the ever improving sophistication of the model calculations also means that running these codes and performing a reliable analysis is rather difficult and requires much experience, which many researchers do not have enough time to gain. It is therefore useful to develop databases of precalculated models. Such databases will free up valuable time for astronomers who could study stellar atmospheres with reasonable accuracy but with fewer time-consuming simulations. Furthermore, these databases will not only accelerate the studies of the large number of observed spectra that are in line for analysis, but also ensure that they are made in a uniform manner (e.g., using the same atomic data). This uniformity will also help to identify and correct possible shortcomings in the codes that were used to produce the database.

The basic parameters of such databases of precalculated models are the surface temperature (T_{eff}), the stellar mass (M), and the surface chemical composition. An adequate analysis of massive stars also has to take into account the parameters associated with the stellar wind, such as the terminal velocity (V_{∞}), the mass-loss rate (\dot{M}), and the clumping. When the variations of all necessary parameters are taken into account, the number of precalculated models that are needed will increase exponentially. Production of such databases is therefore only possible using clusters of computers or supercomputers.

A few databases of synthetic stellar spectra are currently available, but only with a few dozen or some hundred stellar models (see, e.g., Fierro et al. 2015; Hamann & Gräfener 2004; Palacios et al. 2010; Hainich et al. 2019). On the other hand, we here generate a database with tens of thousands of models (Zsargó et al. 2017) that will be publicly available in about January 2021. It will be impossible to manually compare an observed spectrum with this many model calculations. It is therefore imperative to develop tools that allow the automation of this process, but without compromising the quality of the fitting. Fierro-Santillán et al. (2018) presented *FITSpec*, the first of these

tools, that searches our database for models that best fit the observed spectrum in the optical. It uses the Balmer lines to measure the surface gravity ($\log g$) and the equivalent width ratios of the He II and He I lines to estimate the surface temperature (T_{eff}).

In this article we describe the development state of our grid of precalculated models and the results of a test analysis to verify the usefulness of the grid. In § 2 and § 2.1 we briefly describe the stellar atmosphere code (CMFGEN) that we use to produce our models. Next, in § 3 we describe our model grid, and § 4 presents a simple test analysis to demonstrate the benefits that our grid offers. Finally, in § 5 and 6 we summarize our conclusions.

2. CMFGEN

CMFGEN (Hillier 2013; Hillier & Miller 1998, 1999; Puebla et al. 2016) is a sophisticated and widely-used nonlocal thermal equilibrium (non-LTE) stellar atmosphere code. It models the spectrum from the FUV to the radio wavelength range and has been used successfully to model O and B stars, W-R stars, luminous blue variables, and even supernovae. Recently, an experimental version of the code has been developed that included the X-ray region in the analysis (Zsargó et al. 2008; Puebla et al. 2016), but this version has not yet been made public. CMFGEN determines the temperature, the ionization structure, and the level populations for all elements in the stellar atmosphere and wind. It solves the spherical radiative transfer equation in the comoving frame in conjunction with the statistical equilibrium and radiative equilibrium equations. The hydrostatic structure can be computed below the sonic point, allowing the simultaneous treatment of spectral lines formed in the atmosphere, in the stellar wind, and in the transition region between the two. Such features make it particularly well suited to the study of massive OB stars with winds. However, there is a price for this sophistication: a typical CMFGEN simulation takes anywhere between 24 and 36 hours of microprocessor time to complete.

For atomic models, CMFGEN uses the concept of super levels, by which levels of similar energies are grouped together and treated as a single level in the statistical equilibrium equations (see Hillier & Miller 1998, and references therein for more details). The atomic model used in this project includes 37 explicit ions of the different elements, which are summarized in Table 1 together with the levels and super levels included in our model. The atomic data references are given in Herald & Bianchi (2004).

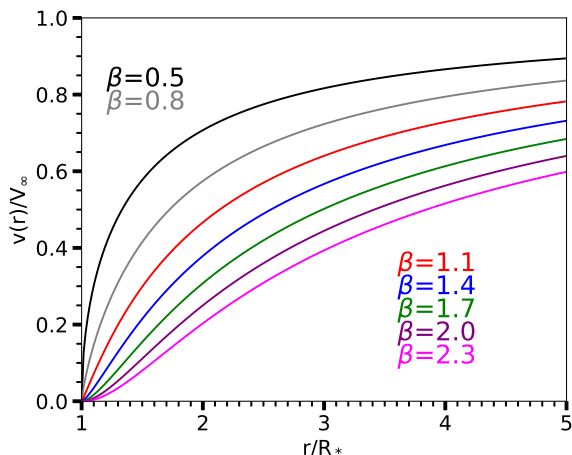
To model the stellar wind, CMFGEN requires values for the mass-loss rate \dot{M} , terminal velocity V_{∞} , β parameter, and the volume filling factor F_{cl} . The profile of the wind speed is modeled by a β -type law (Castor et al. 1975),

$$v(r) = V_{\infty} \left(1 - \frac{r}{R_{\star}} \right)^{\beta}. \quad (1)$$

The β parameter controls how fast the stellar wind is accelerated to reach the terminal velocity (see Fig. 1), while the volume filling factor F_{cl} is the standard method with which the atmospheric models introduce optically thin clumping in the wind (see, e.g., Sundqvist et al. 2014, and references therein). In short, F_{cl} gives the average fraction of a volume element that is filled with material at the outer regions of the wind, where $v(r) \sim V_{\infty}$. Between these regions filled with material, called the clumps, CMFGEN assumes a vacuum. Because of this assumption, we should not expect that our models can reproduce the strong UV lines of the super-ions O VI and N V (see §1 for an explanation). Because

Table 1. Super levels and levels for the different ionization stages included in the models.

Element	I	II	III	IV	V	VI	VII	VIII
H	20/30	1/1
He	45/69	22/30	1/1
C	...	40/92	51/84	59/64	1/1
N	...	45/85	41/82	44/76	41/49	1/1
O	...	54/123	88/170	38/78	32/56	25/31	1/1	...
Si	33/33	22/33	1/1
P	30/90	16/62	1/1
S	24/44	51/142	31/98	28/58	1/1	...
Fe	104/1433	74/540	50/220	44/433	29/153	1/1


Fig. 1. Examples of β -type velocity laws. The curves and the corresponding β values are color-coded.

the continuity equation requires that the average wind density is defined as $\langle \rho \rangle = \dot{M} / [4\pi r^2 v(r)] = \rho_{cl} f_{cl}(r)$, the volume filling factor also tells us how the degree of overdensity in the clumps compares to $\langle \rho \rangle$. In CMFGEN the radial distribution of the volume filling factor is described by the relation

$$f_{cl}(r) = F_{cl} + (1 - F_{cl}) \cdot \exp\left[-\frac{v(r)}{V_{cl}}\right], \quad (2)$$

where the parameter V_{cl} controls how fast F_{cl} is reached in the wind. The lower V_{cl} , the faster and closer to the stellar surface does the volume filling factor reach the value of F_{cl} . During the generation of our models in the grid, we used the generic value $V_{cl} = 0.1 V_{\infty}$.

2.1. Synthetic spectra

The auxiliary program CMF_FLUX of the CMFGEN package (Hillier 2013) computes the synthetic observed spectrum in the observer's frame, which is one of the most important outputs of our models. To simulate the effects of rotation on the spectral lines, the synthetic spectra can also be rotationally broadened using the program ROTIN3, which is part of the TLUSTY package (Hubeny & Lanz 1995).

For each model in the grid, we calculate the normalized spectra in the UV (900-3500 Å), optical (3500-7000 Å), and IR (7000-40 000 Å) range. Then, we can apply rotation by sampling the range between 10 and 350 km s⁻¹ with steps of 10 km s⁻¹.

3. Model grid

In order to properly constrain the input parameters, we used the evolutionary tracks and isochrones of Ekström et al. (2012) calculated with solar metallicity ($Z = 0.014$) at the zero-age main sequence (ZAMS). They computed 24 different evolutionary tracks with initial masses between 0.8 and 120 M_{\odot} as well as 37 isochrones for both rotating and stationary models. The rotating models start on the ZAMS with an equatorial rotational velocity $V_{eq} = 0.4 V_{crit}$ that is later evolved as the star loses angular momentum through mass loss or magnetic braking. The differential rotation within these stars gives rise to meridional circulation that enhances the surface chemical composition by moving CNO-processed material from the interior to the surface. The theory of rotation is described in a series of papers by the Geneva group (Maeder 1999; Maeder & Meynet 2000, and references therein). We refer to these papers for more information.

The predictions of Vink et al. (2001) were used to calculate mass loss for normal early-type stars and lower mass W-R stars, and the recipe of Gräfener & Hamann (2008) was used for massive W-Rs. The evolution was computed until the end of the central carbon-burning phase, the early AGB phase, or the core helium-flash for massive, intermediate, and low- and very low-mass stars, respectively. The initial abundances were those deduced by Asplund et al. (2009), which best fit the observed abundances of massive stars in the solar neighborhood. For each track, Ekström et al. (2012) calculated 400 evolutionary stages and provided the luminosity L , the surface temperature T_{eff} , and the mass M together with mass-loss rates \dot{M} , the surface chemical composition, and the parameters that describe the stellar interior (see Ekström et al. 2012, for more details). This covers all parameters that our models need, except for those that describe the structure of the wind. For the stellar radius and $\log g$ we calculated values that are consistent with their published luminosities L , surface temperatures T_{eff} , and masses M by using the Stefan-Boltzmann law and the assumption of spherical symmetry.

The elements included in our models are H, He, C, N, O, Si, P, S, and Fe. The abundances of H, He, C, N, and O were taken from the tables of Ekström et al. (2012). For consistency, we assumed solar metallicity as reported by Asplund et al. (2009) for Si, P, S, and Fe in all models.

We only had to improvise to describe the wind structure, that is, to determine values for the terminal velocity V_{∞} , β parameter, and volume filling factor F_{cl} . These parameters have no relevance in the evolutionary calculations, therefore no values were reported in Ekström et al. (2012), but they are very important to reproduce observed spectra. The terminal velocity is thought to be related to the escape velocity for hydrodynamical considerations. We therefore used V_{esc} to estimate its values (where V_{esc}

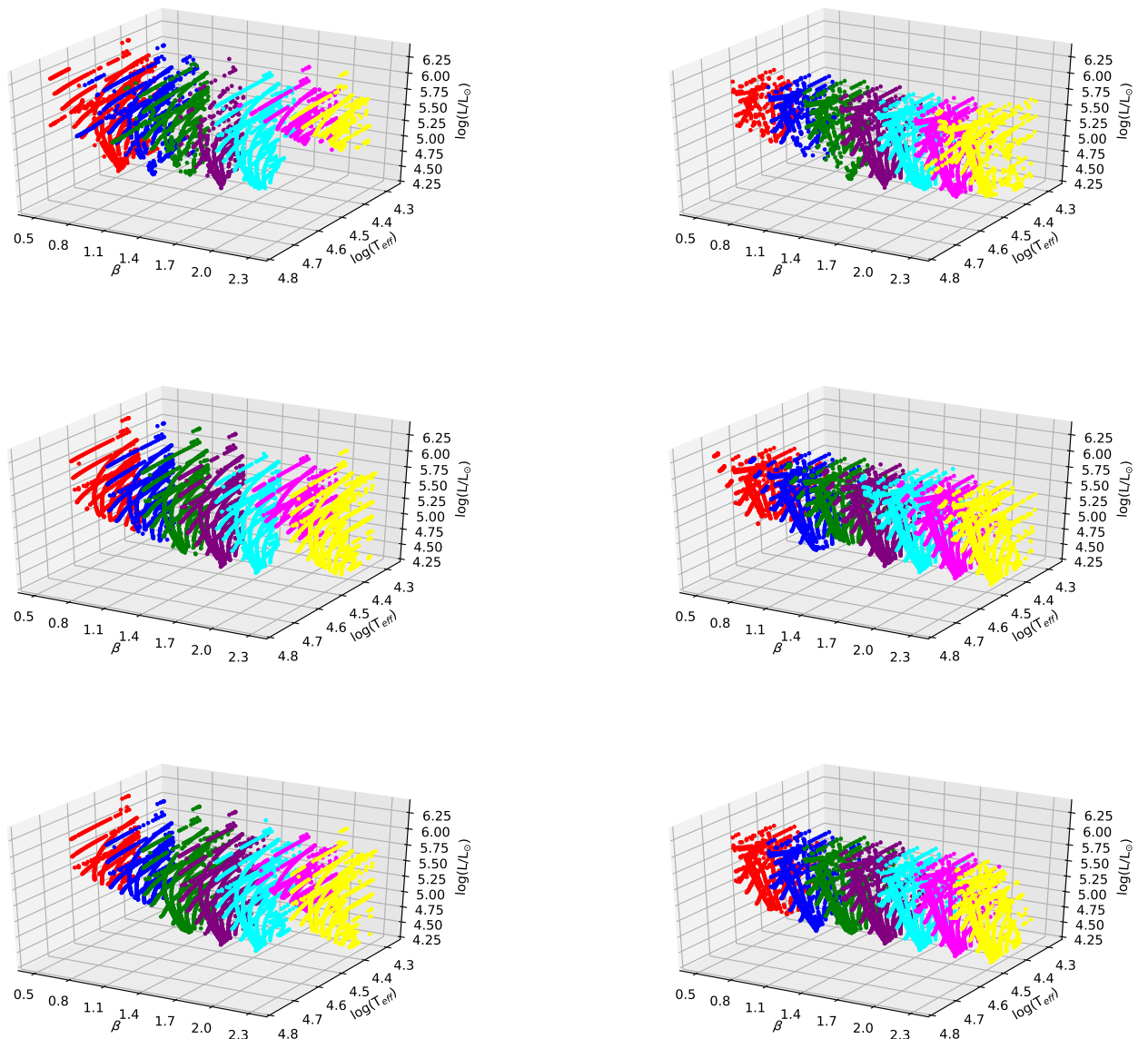


Fig. 2. Hyper-cube plane formed by 3D datacubes. The dimensions of this plane are the different values of the volume filling factor ($F_{cl}=0.05, 0.3$, and 0.6 from top to bottom) and the two metallicities (right column: solar enhanced by rotation; left column: solar without rotational enhancement). Each datacube contains seven H-R diagrams formed by the models in our grid. We used color-coding to help visualize the H-R diagram corresponding to a β parameter.

has its usual meaning). For β and F_{cl} , we simply used the range of values reported in previous studies of massive stars to define the grid.

The grid is organized as hyper-cube data of dimensions that correspond to V_{∞} , F_{cl} , and the metallicity, as illustrated in Fig. 2. For V_{∞} we plan to use two values, a low- ($V_{\infty}=1.3V_{esc}$) and a high- ($V_{\infty}=2.1V_{esc}$) velocity model, to cover the range of terminal velocities reported in the literature. However, up to the preparation of this paper we have only generated models for the higher velocity. The hyper-cube in Fig. 2 therefore has only two dimensions, given by F_{cl} and the metallicity. Each value of the volume filling factor ($F_{cl}=0.05, 0.3, 0.6, 1.0$) combined with one of the two possible values of the metallicity (solar without rotational enhancement and solar enhanced by rotation) generates a datacube that contains a 3D space of models with dimensions

that are defined by β , T_{eff} , and L , as illustrated by Fig. 2. The planes generated by each β parameter (with $\beta=0.5, 0.8, 1.1, 1.4, 1.7, 2.0, 2.3$) within a datacube are the H-R diagrams (see, e.g., Figs. 3–5), where the values of L and T_{eff} are restricted by the evolutionary tracks.

In Figs. 3 to 5 (see also Fig. A.3 in the appendix) we show a sample of the H-R diagrams formed by our models in the datacubes. Obviously, during the generation of our grid we only consider the region in the complete H-R diagram that is relevant for massive stars with line-driven winds (O/B-types and W-Rs), therefore only the upper left part of the full H-R diagram is covered by our models. We do not generate CMFGEN model for each evolutionary stage that is shown in the figures (we do not have the computing resources for this), only for the models that have $\dot{M} > 10^{-8} M_{\odot} \text{yr}^{-1}$. The large blue stars in the figures mark

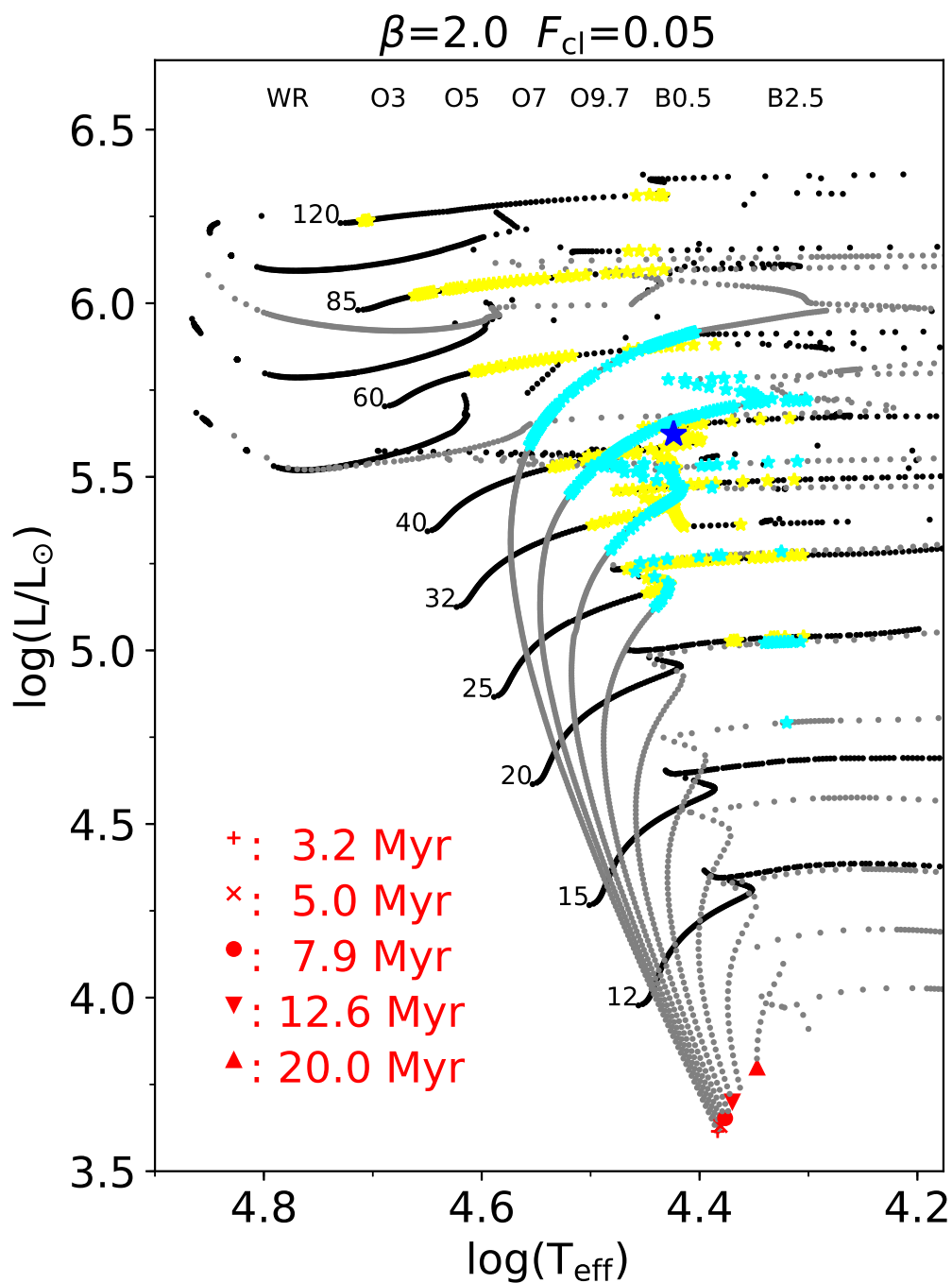


Fig. 3. Hertzsprung-Russell diagram for $\beta=2$, $F_{cl}=0.05$, and solar composition without rotational enhancement. The black and gray symbols mark the evolutionary tracks and isochrones, respectively, calculated by Ekström et al. (2012). We use the stellar parameters from these models, together with our choice of wind parameters, to create the CMFGEN atmospheric models in our grid. The yellow and cyan stars indicate evolutionary track and isochrone models, respectively, for which we have already generated an atmospheric model. The large blue star shows the location of our best-fit model to the observation of ϵ Ori. The numbers left of the evolutionary tracks are the initial masses of the tracks (in M_{\odot}). They also mark the approximate location of the ZAMS. The red symbols below selected isochrones indicate their ages (in 10^6 years). At the top of the figure we indicate the approximate locations of selected spectral classes.

the location of the models that best-fit the observations of ϵ Ori. We discuss the implication of the position of these models in §5.

The coverage of the relevant part of the H-R diagram for the wind parameters is quite diverse, and generally better for intermediate masses than for the extremes. It is also quite clumpy, with clusters of models separated by gaps; this is not ideal for spectral analysis. The reason for this is technical, and it is the

consequence of our strategy of optimizing the production of our models. CMFGEN, like any other code that relies on iterative methods to solve a nonlinear system of equations, needs good initial estimates to achieve secure convergence in reasonable time. Because it is difficult to produce such estimates, the first models (the seed models) in a new region of the parameter space can be quite troublesome. They often fail to converge and can

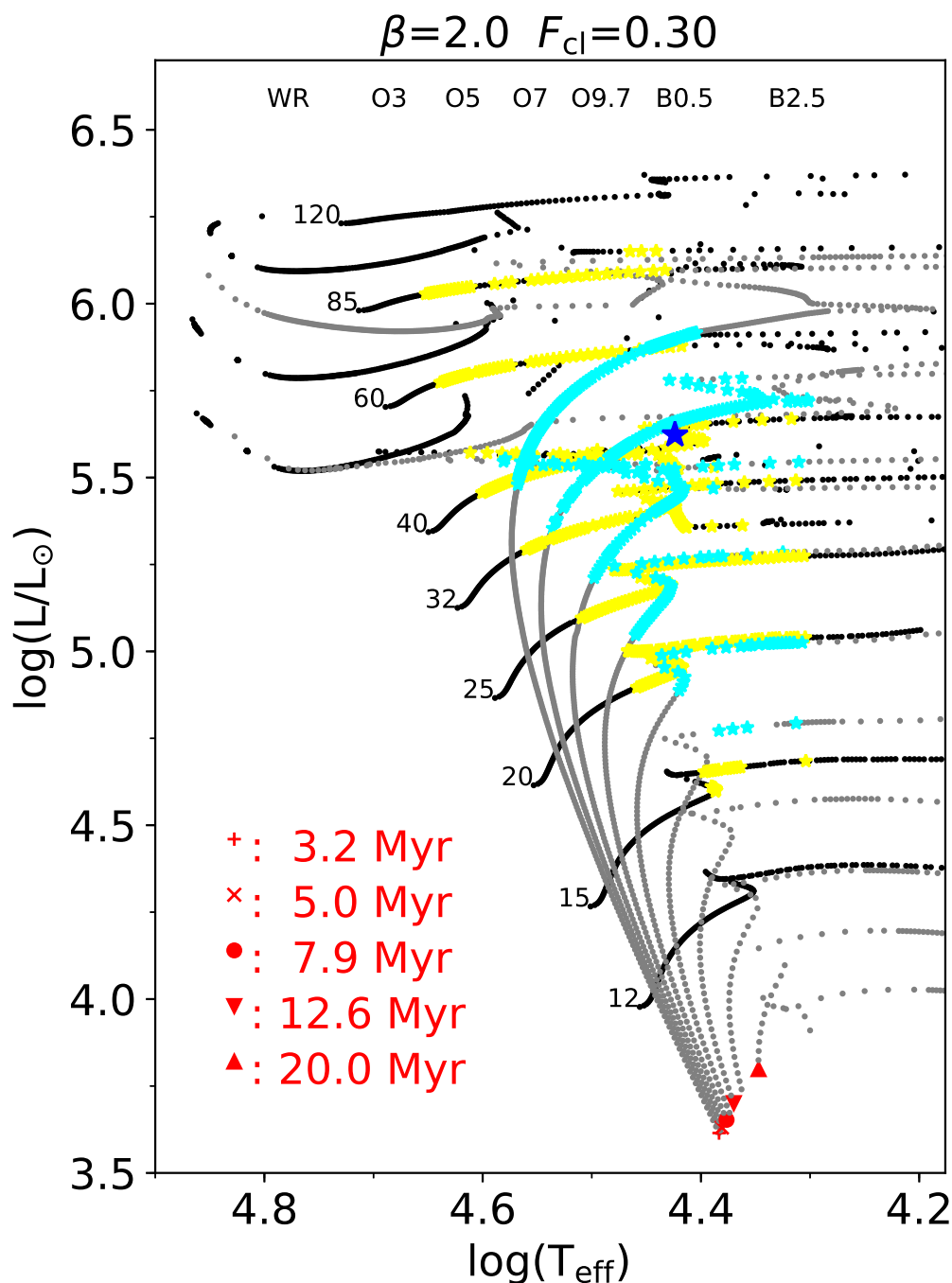


Fig. 4. Same as Fig. 3, but for models with $F_{cl}=0.3$ and solar chemical composition without rotational enhancement.

run 3-4 times longer than a normal model. It is therefore wise to minimize the number of seed models during the generation of the models and grow the grid around existing seed models that can provide good initial conditions for the next generations of models. We use this strategy to optimize the usage of the computing facilities; however, this results in the clumpy distribution of models described above.

We do not show any models for $F_{cl}=1$. The reason for this is clear from Figs. 6 and 7, which show the number distribution of the models as functions of the F_{cl} and β parameters. Our coverage for all other F_{cl} volume filling factors is decent and we have many models (43,340), but not for $F_{cl}=1$. The coverage for this

volume filling factor is so low that it is pointless to show any H-R diagrams. Fortunately, it is highly unlikely that modelers encounter a wind that has no density structures (clumps) at all. Calculations with $F_{cl}=1$ therefore had low priorities so far, hence the low number of models. Nevertheless, these models will be produced and will be available in the completed grid.

Despite the shortcomings, the grid has already reached a level at which it can be used for real analysis. We are therefore in the process of making it available on the internet, together with the tools that we can currently offer to use it. It will be freely available for any interested researcher by the end of 2020.

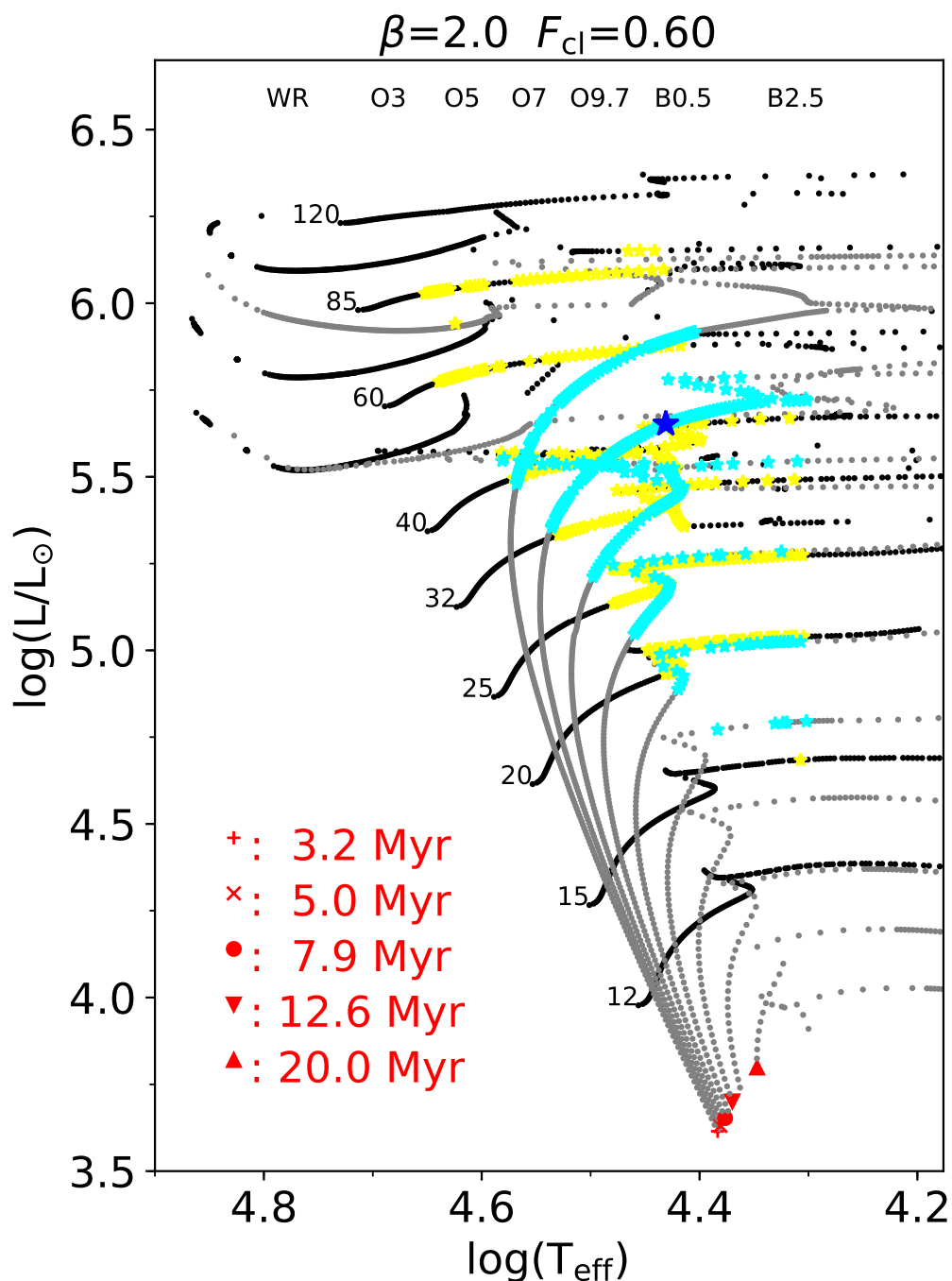


Fig. 5. Same as Fig. 3, but for models with $F_{cl}=0.6$ and solar chemical composition without rotational enhancement.

Finally, we would like to justify our choices of parameters and comment on future expansions of the grid. It might rightfully be argued that we ignore some important parameters in the grid. The most consequential omission is the turbulent velocity because it affects the analysis of optical He lines. Instead of exploring these effects, we simply use a generic $V_{\text{turb}}=20 \text{ km s}^{-1}$ throughout the wind. Furthermore, we should not really use the same ionic species for the hottest O-type and for the B-type stars because the ionization level of elements can be different for these stars (the most notable example is Fe). However, we have limited access to the computational resources, and compromises and hard choices have to be made. With our selection of parameter

space, we intend to create a grid that is sophisticated enough to be useful in the analysis of observed spectra, but the computational requirements of its production stay within the limits. It is not a trivial task to achieve this compromise because the limits can easily be exceeded by introducing a seemingly minor adjustment in the parameter space.

Nevertheless, if there is future demand for an expansion of the parameter space (e.g., have a range in turbulent velocity), we will address it with a follow-up project. The grid can be augmented in the future, and not only by us, if sufficient computing resources are available. Furthermore, there are ways to improve our grid that do not involve running more models on supercom-

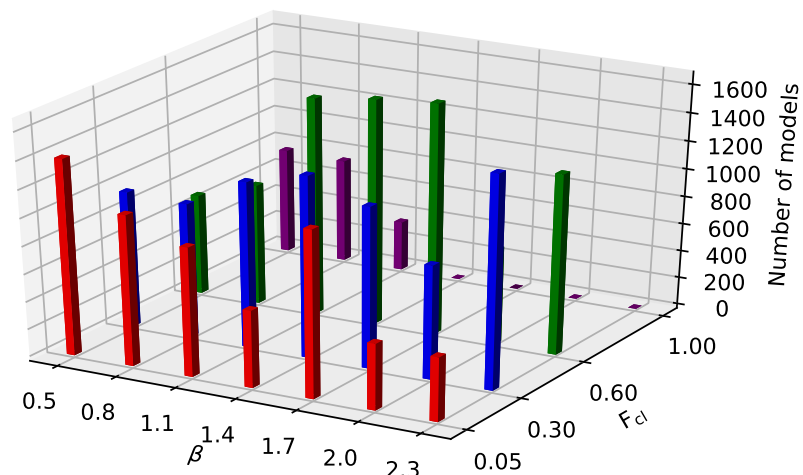


Fig. 6. Distribution of the 24,423 models with no rotational enhancement that are currently available as functions of wind parameters. The color-coding is to help visualize the models that correspond to the same F_{cl} volume filling factor.

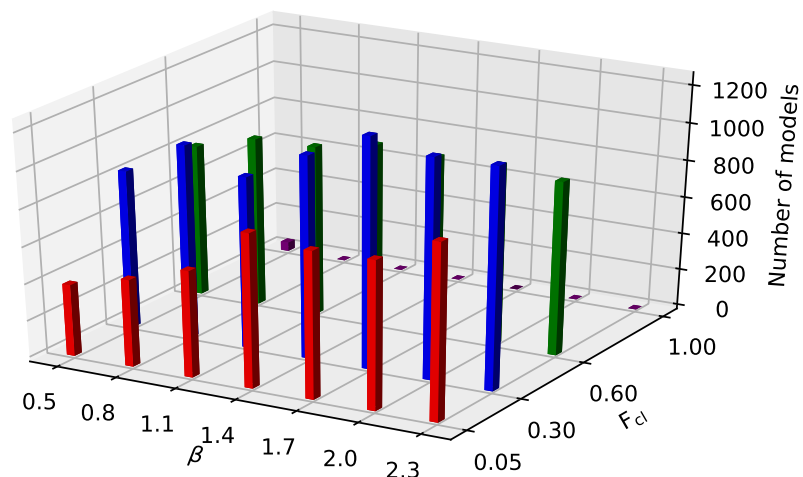


Fig. 7. Same as Fig. 6, but for the 18,917 models with rotational enhancement that are currently available in the grid.

puters. We can, for example, appeal to the users of CMFGEN to donate their no longer needed models to the grid. We suspect that there are hundreds or even thousands of models sitting idle in computers around the world. Including such a diverse set of models into our grid will be challenging, but might be feasible.

We describe our choice of parameter space in the context of the intended purpose of the grid. We wish to provide a tool for easy and rapid analysis of the stellar spectra that will serve well a variety of special applications where the need for rapid analysis outweighs the need for high-accuracy parameter determination. Examples of such applications include statistical analyses of large stellar samples or population synthesis models. However, we do not mean to replace the traditional modeling by using

only the grid for a detailed analysis of a particular star. In such cases, the investigators still have to fine-tune the parameters by running models with the code of their preference (which does not have to be CMFGEN) to complete the task. Using the grid will speed up the analysis by eliminating the need to run numerically costly seed models in the early phases of the investigation, and will provide good initial conditions for the fine-tuning phase. The time saving is very significant. For example, our reanalysis of ϵ Ori lasted only about two days, while the duration of the original work by Puebla et al. (2016) was several weeks. We are talking about a five- to tenfold decrease in the required time.

4. Simple test to demonstrate the usefulness of our grid

We demonstrate the benefits that our grid offers by reanalyzing ϵ Ori. This B0 Ia supergiant was recently studied by Puebla et al. (2016) in the traditional way, that is, by producing every model that was needed for the analysis. Some members of our team were part of the group that performed this study, and so they had access to the observational data used in the work of Puebla et al. (2016). It is therefore convenient and very useful to see the result we would obtain by using the models available in our grid and without running CMFGEN at all. Before presenting our results, we have to mention some limitations that our reanalysis has in comparison with the original study. For example, Puebla et al. (2016) used the experimental version of CMFGEN and included high-resolution X-ray observations in the analysis to augment the UV and optical spectra. Because we are used the commonly available version of CMFGEN, we cannot reproduce their results in the X-ray range and so we cannot verify the additional information gained by using this spectral range (e.g., additional constraints on the mass-loss rate and abundances). Furthermore, our models assume vacuum in the interclump medium, as opposed to theirs, which included tenuous but not empty regions between the clumps. By doing so, they successfully reproduced the FUV O VI and N V lines, which we were not able to do. Nevertheless, in the following sections we demonstrate that we can reproduce their results quite well and that process in a spectral analysis can be made by using our grid and before running any simulation.

Finally, we note that because we used the very same observations in our analysis as Puebla et al. (2016) did, we omit the description of the data reduction and the observations in this paper. We refer to the relevant sections of Puebla et al. (2016) for more information on this subject.

4.1. ϵ Ori (HD37128)

This supergiant star is the central star of the Orion belt and belongs to the Orion OB1 association. It has been studied many times in the past. The most recent works include Kudritzki et al. (1999), who found $T_{\text{eff}} = 28,000$ K and $\log g = 3.00$ for this star using the code FASTWIND, as well as a series of CMFGEN studies by Crowther et al. (2006), Searle et al. (2008), and Puebla et al. (2016). The first two authors found very similar effective temperatures, that is, 27,000 and 27,500 K, respectively, but they diverged significantly in the value of $\log g$ (2.9 and 3.1, respectively). Previous studies also reported a wide range of mass-loss rates, but in general, lower than $5.0 \times 10^{-6} M_{\odot} \text{ yr}^{-1}$. The majority of these studies assumed smooth wind (no clumping).

However, the most relevant results for our analysis are those found by Puebla et al. (2016). They reported $T_{\text{eff}} = 27,000 \pm 500$ K, $\log g = 3.00 \pm 0.05$, a mass-loss rate of $\dot{M} \sim 10^{-7} M_{\odot} \text{ yr}^{-1}$, $V_{\infty} \sim 1800$ km s^{-1} , and a highly clumped and slowly accelerating wind ($F_{\text{cl}} = 0.01$, $\beta > 2.0$) for ϵ Ori. However, their volume filling factor is not really well defined because of uncertainties in considering the degree to which the UV lines are affected by the velocity-space porosity. If they are not affected too much, the wind has to be very clumped and the mass-loss rate has to be low in order to fit the S IV $\lambda\lambda 1062, 1073$ and the P V $\lambda\lambda 1118, 1128$ profiles. Because of this uncertainty, the authors considered four variations of the same model with $F_{\text{cl}} = 0.01, 0.05, 0.1$, and 1.0 as their best models, each with mass-loss rates adjusted to conserve the ratio $\dot{M} / \sqrt{F_{\text{cl}}} \sim 1.6 \times 10^{-6} M_{\odot} \text{ yr}^{-1}$. We refer to their Tables 4 and 5 to learn more about their best results.

Table 2. Weights used by FITspec for ϵ Ori.

Lines or ratios	Initial weights	Final weights
T_{eff} fit:		
He II 4541/He I 4471	0.25	0.20
He II 4200/He I 4026	0.25	0.30
He II 4200/He I 4144	0.25	0.30
He II 4541/He I 4387	0.25	0.20
$\log g$ fit:		
H I 3835	0.17	0.17
H I 3889	0.17	0.17
H I 3970	0.17	0.17
H I 4102	0.17	0.17
H I 4341	0.17	0.16
H I 4861	0.17	0.16
Combined fit:		
Ratios He II/He I	0.50	0.50
EWs H I	0.50	0.50

4.2. Analysis by FITspec

As previously mentioned, we intend to provide tools that aid the comparison of the model and observed spectra and accelerate the search for the best-fitting models. FITspec, the first of these tools, is already operational, therefore it is natural to start our reanalysis of ϵ Ori by applying this code. To start an analysis by FITspec, the user must measure the equivalent widths (EWs) in the observations of the $\lambda\lambda 3835, 3889, 3970, 4101, 4349, 4861$ lines of the H Balmer series, and those of the He II $\lambda\lambda 4541$ and 4200, as well as the He I $\lambda\lambda 4471, 4387, 4144$, and the He I+He II blend at $\lambda 4026$; and provide them as inputs. The program then compare these EWs with those measured in the models and finds the closest match. This procedure is relatively fast because FITspec has a complete library of the EWs for these lines measured in each model spectra of the grid. Instrumental and rotational broadening of the observed spectra are not of concern because they do not affect the measured EWs.

FITspec uses the EW of the Balmer lines and the EW ratios of He II and He I lines to search for the best-fitting models in the $\log g - T_{\text{eff}}$ space. The strategy is the following. First, the code calculates the ratios of

$$\frac{\text{EW}(\text{He II } \lambda 4541)}{\text{EW}(\text{He I } \lambda 4471)}, \quad (3)$$

$$\frac{\text{EW}(\text{He II } \lambda 4200)}{\text{EW}(\text{He I } \lambda 4026)}, \quad (4)$$

$$\frac{\text{EW}(\text{He II } \lambda 4200)}{\text{EW}(\text{He I } \lambda 4144)}, \quad (5)$$

$$\frac{\text{EW}(\text{He II } \lambda 4541)}{\text{EW}(\text{He I } \lambda 4387)}, \quad (6)$$

then the relative differences, or as we call them, the "errors", are calculated by

$$\text{Error}_{\text{EW}} = \frac{\text{EW}_{\text{obs}} - \text{EW}_{\text{model}}}{\text{EW}_{\text{obs}}}, \quad (7)$$

for each H Balmer line, and by

$$\text{Error} \left(\frac{\text{He II}}{\text{He I}} \right) = \frac{\left(\frac{\text{He II}}{\text{He I}} \right)_{\text{obs}} - \left(\frac{\text{He II}}{\text{He I}} \right)_{\text{model}}}{\left(\frac{\text{He II}}{\text{He I}} \right)_{\text{obs}}}. \quad (8)$$

Table 3. Models in the grid that best fit the observations of ϵ Ori

Parameter	Model 1	Model 2	Model 3
T_{eff} (K)	26,540	26,540	26,980
L ($10^5 L_{\odot}$)	4.196	4.196	4.491
$\log g$	3.02	3.02	3.06
R (R_{\odot})	30.62	30.62	30.65
\dot{M} ($10^{-7} M_{\odot} \text{yr}^{-1}$)	1.526	3.737	10.82
V_{∞} (km s^{-1})	1,414	1,414	1,473
β	2.0	2.0	2.0
F_{cl}	0.05	0.3	0.6
$v \sin i$ (km s^{-1})	80	80	80
M_{ini}^a (M_{\odot})	40	40	44
Age^a (10^6yr)	4.47	4.47	3.98
$X(\text{He})^a$	0.266	0.266	0.266
$X(\text{C})^a$	2.31E-3	2.31E-3	2.31E-3
$X(\text{N})^a$	6.59E-4	6.59E-4	6.59E-4
$X(\text{O})^a$	5.73E-3	5.73E-3	5.74E-3
Chemical comp. ^a	Solar without rotational enhancement		

^aFrom the evolutionary models of Ekström et al. (2012).

for each He II to He I ratios defined by Eqs. (3)–(6).

FIT $spec$ then calculates the weighted averages of these errors, where the weights need to be specified by the user a priori. Weights are usually assigned to lines that reflect the quality of their signal-to-noise ratio (S/N) (see Table 2 for the weights we used for ϵ Ori). Then, models with average errors smaller than 30% in either the EWs of the H Balmer lines or the EW ratios of the He lines are selected, and among these models FIT $spec$ identifies the model that has the smallest total error,

$$\text{Error}_{\text{tot}} = \sqrt{\sum (\text{Error}_{\text{EW}})^2 + \sum \left[\text{Error} \left(\frac{\text{He II}}{\text{He I}} \right) \right]^2}, \quad (9)$$

where the summation is over all H lines and He ratios. Then, the user has the option to adjust the weights, if necessary, and restart the procedure. After a few iterations, the best-fitting models are found. More about the code FIT $spec$ and the way it works can be found in Fierro-Santillán et al. (2018).

After running FIT $spec$, we found that models with $T_{\text{eff}}=27,320 \pm 1500$ K and $\log g=3.27 \pm 0.29$ fit the observations best that agree very well with the results of previous studies.

4.3. Visual inspection of the spectra

After identifying the relevant parameter ranges in T_{eff} and $\log g$ by FIT $spec$, we visually inspected the models within these ranges. This was done with another tool that we created to help in the search for best-fitting models. The tool allows selecting specific lines from any wavelength region for display on the screen and compare the observations with selected models. The display is very similar to Fig. 9, for example. Several of our figures are simple snapshots of this display. Then, we can browse through a number of models and visually inspect the fit. The user has the option of changing the parameter ranges of the models that are queued for inspection, to apply rotational or instrumental broadening to the model spectra, to Doppler-shift them, zoom in and out, and the displayed lines can also be changed. The comparison can be made in the form of normalized or calibrated flux spectra. Unfortunately, the interaction with the code is not yet user-friendly, therefore we have not yet released it. However, we

are developing a graphic user interface to make it user friendly. When this code is optimized and easy to apply, it will be released and will be a powerful tool if used in combination with FIT $spec$.

With the help of FIT $spec$ we were able to decrease the number of models that are to be inspected visually to a few hundred, and then applied a rotational broadening with $v \sin i=80$ km s^{-1} . The convolution of the model spectra with a broadening profile adequately accounts for the rotation and macro-turbulence for slowly rotating stars (Hillier et al. 2012). Wind-free line profiles were used to estimate the projected rotational velocity $v \sin i$. After several hours of inspection, we then found that $26,500 \text{ K} < T_{\text{eff}} < 27,000 \text{ K}$, $3.0 < \log g < 3.1$, $\beta=2.0 \pm 0.3$, and $V_{\infty} \geq 1500 \text{ km s}^{-1}$ are the best values for the stellar and wind parameters (see the parameters of the best-fitting models in Table 3). The error estimates are based on the ranges of acceptable models and on the parameter resolutions that we have in the grid. Unfortunately, we were only able to derive a lower limit for V_{∞} because the coverage that our grid still has in this parameter is limited. For the mass-loss rates we found that \dot{M} could vary between $1.5 \times 10^{-7} M_{\odot} \text{yr}^{-1}$ and $1.1 \times 10^{-6} M_{\odot} \text{yr}^{-1}$, depending on the adopted F_{cl} so that $\dot{M} / \sqrt{F_{\text{cl}}} \sim 1.4 \times 10^{-6} M_{\odot} \text{yr}^{-1}$ is approximately conserved. Our analysis mildly favors the combination of $\dot{M}=1.1 \times 10^{-6} M_{\odot} \text{yr}^{-1}$ with $F_{\text{cl}}=0.6$ and indirectly suggests that vorosity highly affects the UV resonance lines (see the discussion in §5). These values agree well with the results of previous studies. Figs. 8–13 show our best-fitting models with the observed spectra for important H, He, C, N, O, and S lines. In the following, we discuss how the different parameters affect the spectral diagnostics and describe our results.

Fig. 8 shows how well our models fit the Balmer series of hydrogen, especially the model with the highest mass-loss rate (Model 3 in Table 3 and the dashed black lines in Fig. 8). The Balmer series is normally used to measure $\log g$, but the figure reveals that other parameters also affect the H lines. For example, there is a significant effect due to mass loss as the absorption profiles of $H\alpha$ and $H\beta$ are filled in by the emission from the wind. We also observe significant differences in the synthetic profiles for different values of F_{cl} , especially in the case of $H\alpha$. However, the line profiles should not vary with F_{cl} if the mass-loss rate is adjusted to conserve $\dot{M} / \sqrt{F_{\text{cl}}}$. As we explain in § 5, because of the way in which CMFGEN introduces clumping (see Eq. (2)) and the slow acceleration of the wind of ϵ Ori, an extended transition zone exists between the smooth wind near the stellar surface and the outer region with constant F_{cl} . This transition zone has a profound effect on the profiles of the lower order Balmer lines. Fortunately, the effects of the wind emission are negligible on the higher order Balmer lines, as Fig. 8 clearly shows, so we can use them to measure $\log g$. The good fit between the models and the observations in the wings of these lines (see the top panels of Fig. 8) suggests that the most probable value of $\log g$ is about 3.

Fig. 9 shows the comparison of our best-fitting models with the optical He I and He II lines observed for ϵ Ori. Although the He II lines are very weak for this star, the comparison clearly indicates that T_{eff} has to be about 27,000 K. No other parameter significantly affects the He lines, at least in the parameter space that we use in our grid. The derived T_{eff} is also consistent with the observed C, N, O, and S lines, as illustrated by Figs. 10–13. These figures show lines that originate from consecutive ionization levels and do not suggest that T_{eff} needs to be revised. The fit is surprisingly good considering the limited resolution and covering that our grid has in the parameter space. Figs. 11–13 also indicate that the abundances of N, O, and S are about right in the best-fitting models, while Fig. 10 suggests that we should

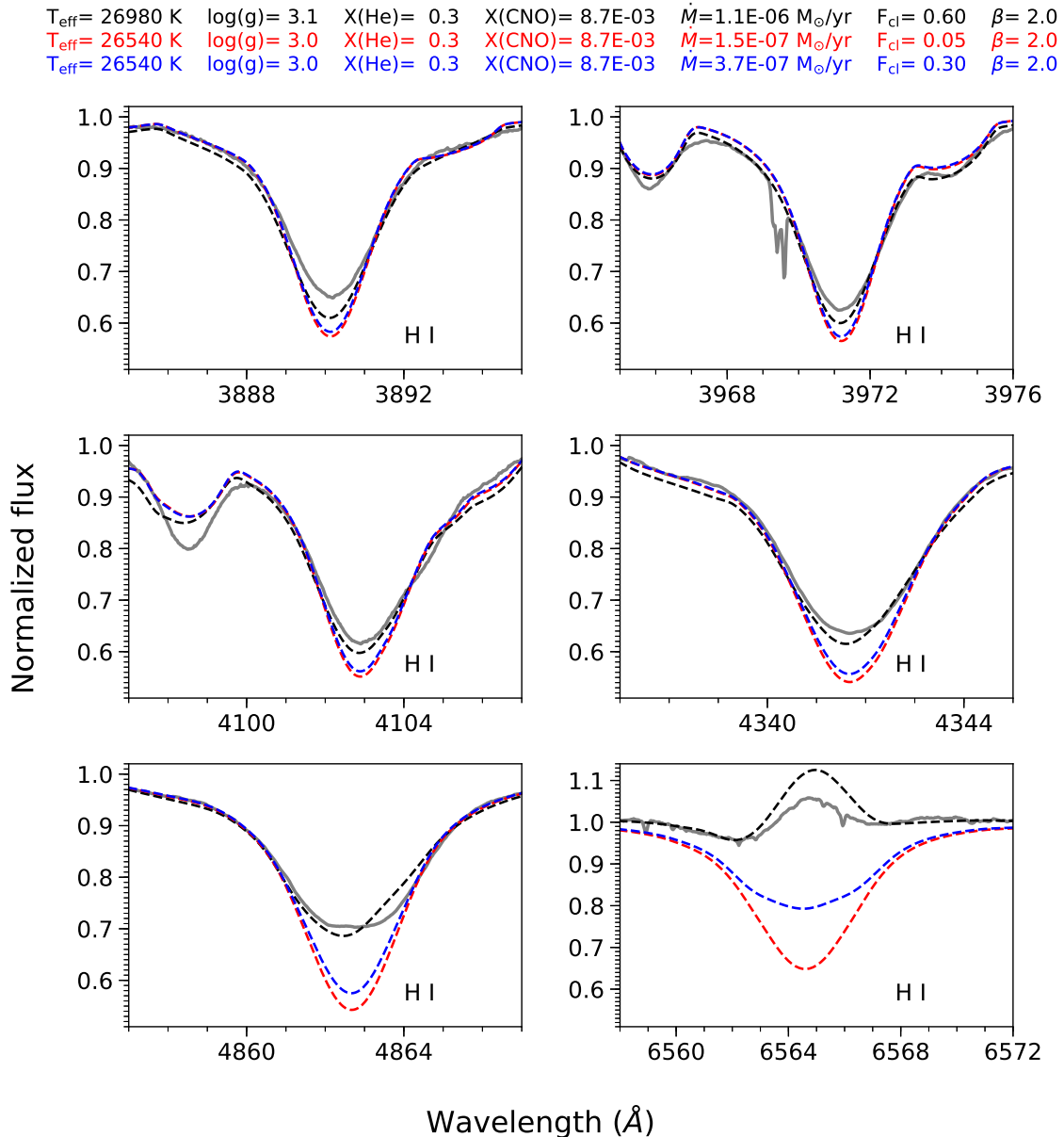


Fig. 8. Comparison of our best-fitting models (dashed black, red, and blue lines) with the observed H I lines for ϵ Ori (solid gray line). The relevant model parameters are color-coded above the panels.

lower the carbon abundance by a factor of few. In this figure all synthetic profiles are stronger than the observations, regardless of the level of ionization. This conclusion agrees very well with the findings of Puebla et al. (2016), who needed a C abundance a factor of 2 to 4 lower than those in our models to fit these lines. However, the objective of this paper is to show how closely we can match the right stellar and wind parameters by using only the grid, therefore we did not adjust the carbon abundance.

The most useful spectral region to estimate the mass-loss rate \dot{M} and terminal velocity V_{∞} is the UV region. Here, we encounter strong resonance lines of the dominant ionization states in the winds of massive stars. These resonance lines often show P-Cygni profiles, which are useful for measuring \dot{M} and V_{∞} (see, e.g., the C IV doublet around 1550 Å or the Si IV doublet around 1400 Å in Fig. 14). Unfortunately, we cannot reproduce many of these lines well for various reasons. For example,

we have a problem to fit the N V doublet around 1240 Å because our models do not include interclump medium. The UV region is also not useful for estimating the β -parameter and F_{cl} because most of the P-Cygni profiles are saturated (and probably strongly affected by vorosity). To derive mass-loss rates, the UV spectra show a somewhat contradictory situation. While the Si IV $\lambda\lambda 1394, 1403$ doublet suggests low values of \dot{M} to fit the C IV $\lambda\lambda 1548, 1550$ we would need much higher mass-loss rates. However, $\dot{M} > 1.5 \times 10^{-6} \text{ M}_{\odot}/\text{yr}^{-1}$ would result in H α emission, which is not observed. We therefore conclude that $1.1 \times 10^{-6} \text{ M}_{\odot}/\text{yr}^{-1} > \dot{M} > 10^{-7} \text{ M}_{\odot}/\text{yr}^{-1}$ is the best estimate we can have. The actual value depends on the adopted F_{cl} . Fig. 14 also shows that the terminal velocity has to be higher than 1,500 km s $^{-1}$, but our grid does not yet have the necessary coverage in V_{∞} to determine its exact value.

$T_{\text{eff}} = 26980 \text{ K}$	$\log(g) = 3.1$	$X(\text{He}) = 0.3$	$X(\text{CNO}) = 8.7\text{E-}03$	$\dot{M} = 1.1\text{E-}06 M_{\odot}/\text{yr}$	$F_{\text{cl}} = 0.60$	$\beta = 2.0$
$T_{\text{eff}} = 26540 \text{ K}$	$\log(g) = 3.0$	$X(\text{He}) = 0.3$	$X(\text{CNO}) = 8.7\text{E-}03$	$\dot{M} = 1.5\text{E-}07 M_{\odot}/\text{yr}$	$F_{\text{cl}} = 0.05$	$\beta = 2.0$
$T_{\text{eff}} = 26540 \text{ K}$	$\log(g) = 3.0$	$X(\text{He}) = 0.3$	$X(\text{CNO}) = 8.7\text{E-}03$	$\dot{M} = 3.7\text{E-}07 M_{\odot}/\text{yr}$	$F_{\text{cl}} = 0.30$	$\beta = 2.0$

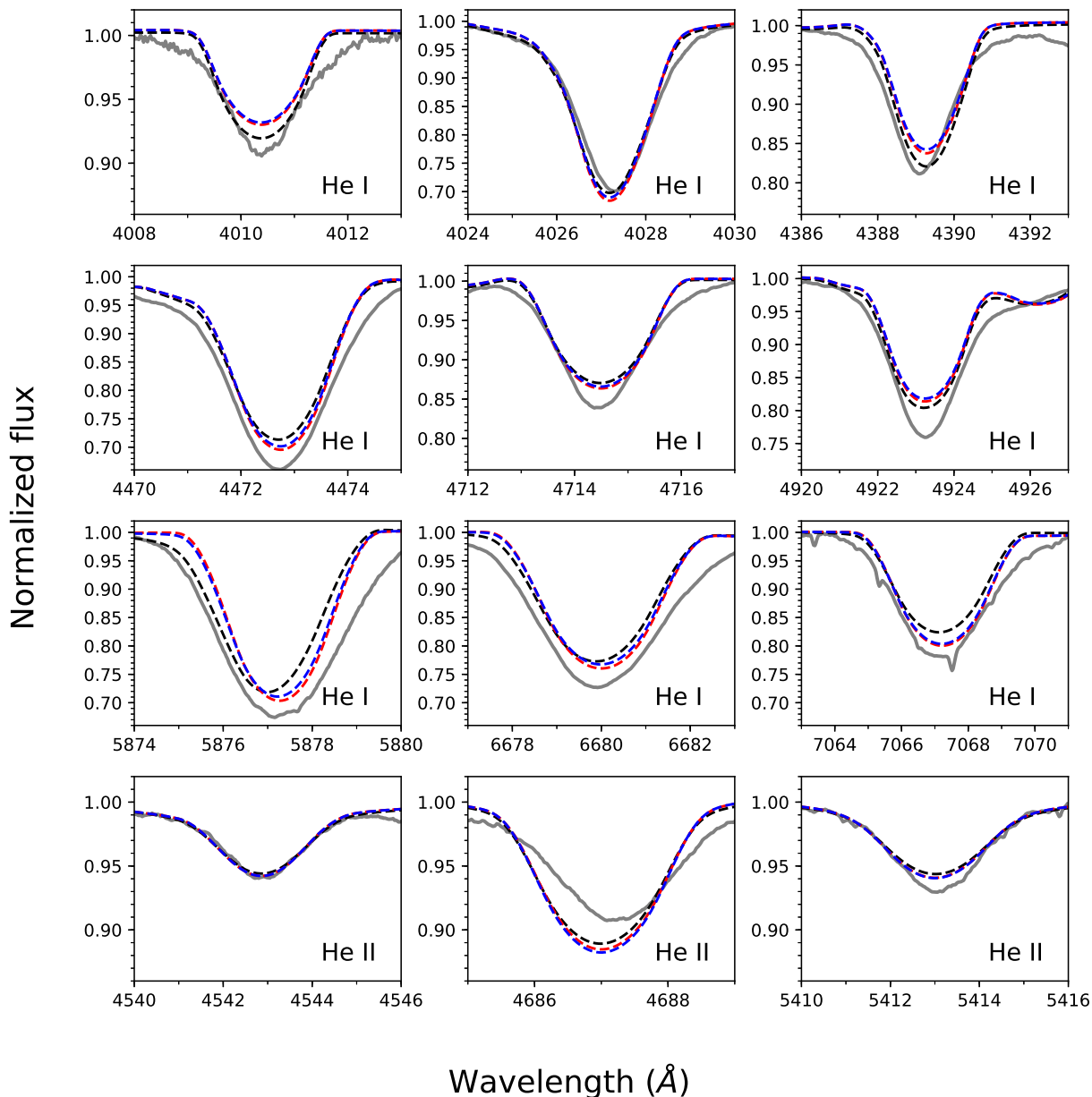


Fig. 9. Same as Fig. 8, but the comparison is for the He I and He II lines.

5. Discussion

In Figs. A.1 and A.2 we show the general comparisons of our best models (dashed black, red, and blue lines) with the observations (gray lines). With these figures we intended to reproduce Figs. A1–A3 in the appendix of Puebla et al. (2016) for an easy comparison of our and their results. These figures also show that the overall fit in the optical range is very good, especially for the model with $\dot{M} = 1.1 \times 10^{-6} M_{\odot} \text{ yr}^{-1}$ and $F_{\text{cl}} = 0.6$. However, as was mentioned earlier, there are significant discrepancies in the UV.

The top panel of Fig. 14 shows that our models lack the O VI profile around 1032 \AA , which is expected because our models do

not take the interclump medium into account. A graver problem is that S IV around 1070 \AA is too strong for our models, especially for $\dot{M} = 1.1 \times 10^{-6} M_{\odot} \text{ yr}^{-1}$ and $F_{\text{cl}} = 0.6$. The same problem led Puebla et al. (2016) to the conclusion that the wind is extremely clumped ($F_{\text{cl}} \sim 0.01$) and \dot{M} is low. However, they have already raised the possibility that the fact that CMFGEN does not yet take the velocity-space porosity into account might be responsible for the anomalously strong S IV profiles in the models. Since the publication of their paper, several studies have concluded that the UV P-Cygni profiles should indeed be affected strongly by the vorosity effects. For example, one of the main conclusion of Sundqvist & Puls (2018) was that velocity-space porosity is critical (in their words) for the analysis of UV reso-

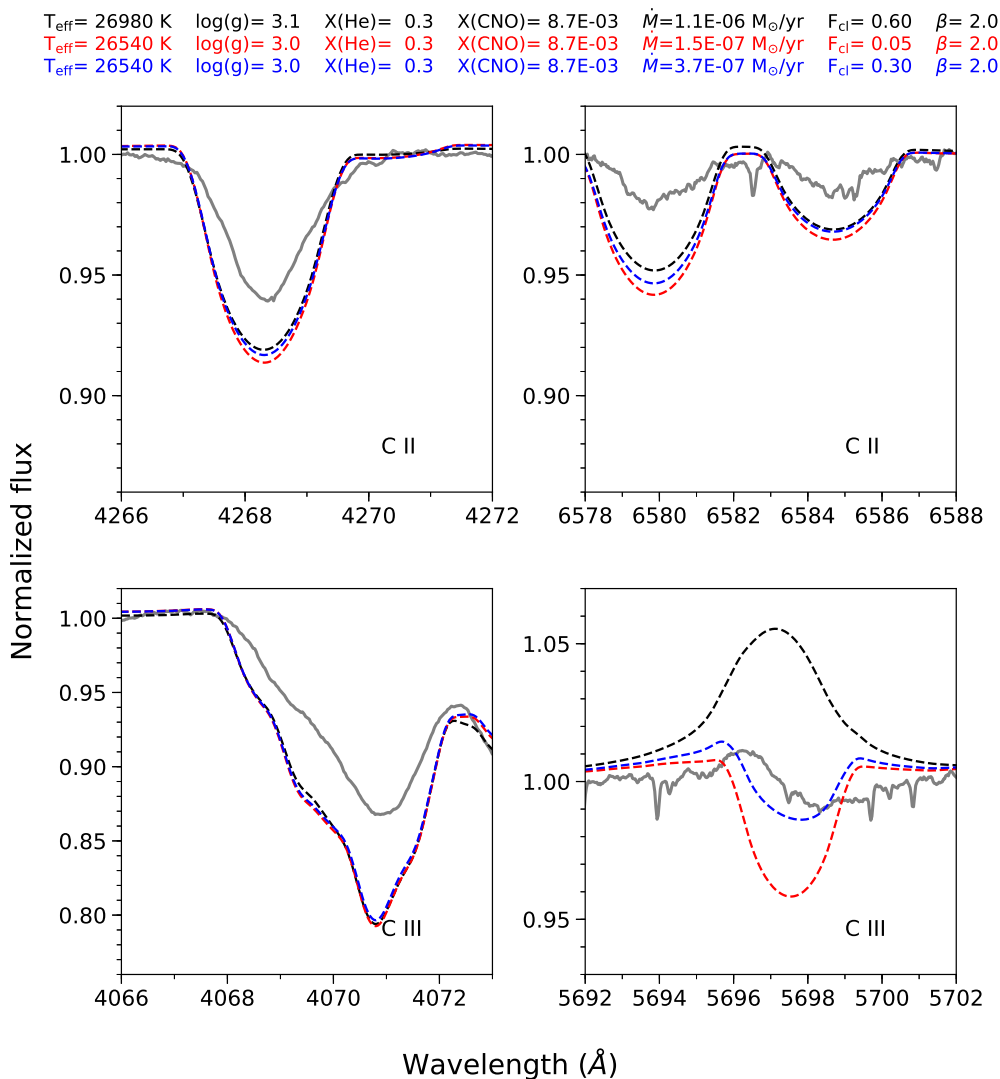


Fig. 10. Same as Fig. 8, but the comparison is for selected C lines.

nance lines in O stars. Taking these effects into account might fix our problems because it would weaken these lines for the same \dot{M} . In short, the theory of velocity-space porosity assumes that as the material is swept up in dense clumps, the process also creates gaps in the velocity distribution of the material. These gaps then allow the escape of radiation that otherwise would be absorbed in smooth wind.

A possible other solution for the weak P-Cygni profiles in the observations could be the low abundances of the species in question. This possibility was raised and quickly dismissed when the same problem was encountered with the P V $\lambda\lambda 1118, 1128$ lines in the spectral analysis of early-O stars. Although we did not adjust abundances in our work, there is nothing in other spectral regions that would suggest anomalously low abundances. The sulphur lines shown in Fig. 13 suggest that the sulphur abundance is more or less correct in our models.

Fig. A.2 and also Fig. 8 illustrate how difficult it is to estimate the parameters F_{cl} and β . We have essentially one diagnostic, $H\alpha$, which is affected by multiple other parameters. Fitting $H\alpha$ is also where our results differ the most from those of Puebla et al. (2016). They found that the highly clumped wind ($F_{\text{cl}} < 0.05$) fits this line the best, while our results suggest a

much lower degree of clumping ($F_{\text{cl}} \sim 0.6$) and a higher mass-loss rate. Most of the difference originates from the different radial distribution of the true volume filling factor, $f_{\text{cl}}(r)$, in our models (see Eq. (2) for its definition). While we use a generic value $V_{\text{cl}} = 0.1V_{\infty}$ in Eq. (2), they used a very low value of $V_{\text{cl}} \sim 50 \text{ km s}^{-1}$. The value we use creates a large transitional zone at the base of the wind for slowly accelerating models ($\beta > 1.7$), while their models always reach the prescribed volume filling factor very rapidly. F_{cl} is the volume filling factor at large radii, where $v(r) \sim V_{\infty}$ in the parameterization of CM-FGEN, and it does not mean that $f_{\text{cl}}(r) = F_{\text{cl}}$ at every radius. In Fig. 15 we show the true radial distribution of $\dot{M} / \sqrt{f_{\text{cl}}(r)}$ calculated by using our best-fitting β and V_{cl} parameters for a typical O star, and what these models would have if we had used the V_{cl} value of Puebla et al. (2016). The quantity $\dot{M} / \sqrt{f_{\text{cl}}(r)}$ is important because it controls the emission by the recombination of H II in the wind (assuming that the ionization structure of hydrogen is similar in the models). The panels in Fig. 15 show that the values of $\dot{M} / \sqrt{f_{\text{cl}}(r)}$ are always higher at every radius for models with smaller V_{cl} (and with all other parameters being the same), and this excess is greater and extends to much larger radii for highly clumped (low F_{cl}) and slowly accelerating (high β) mod-

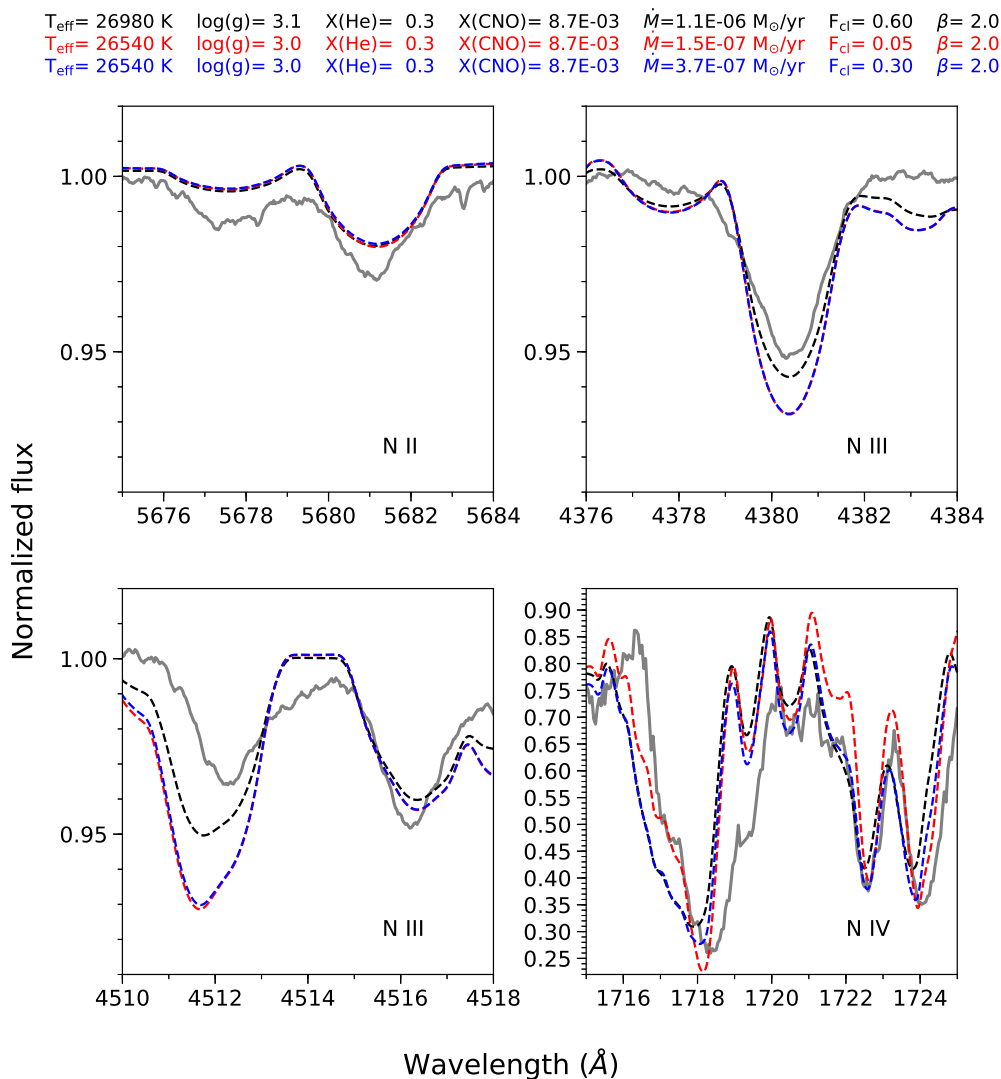


Fig. 11. Same as Fig. 8, but the comparison is for selected N lines.

els. This means that the models of Puebla et al. (2016) produce much more emission in the crucial dense internal part of the wind than ours, especially for smaller F_{cl} and larger β . This explains why our results favor a higher mass-loss rate and a lower level of clumping when the same $\text{H}\alpha$ profile is analyzed. Finally, we would like to stress that the difference would be smaller if the wind of ϵ Ori had accelerated normally ($\beta < 1$).

It is difficult to judge which distribution is more realistic because the hydrodynamic simulations are quite fuzzy on this subject (see, e.g., Runacres & Owocki 2002). The simulations suggest that the wind is smooth near the stellar surface and predict a transitional zone, but they are not clear about the size of this zone. The motivation behind using an Eq. (2) type distribution is exactly to reproduce these characteristics and to recognize that the clumping scales with the wind velocity, that is, the faster the wind, the more clumped. The wind of ϵ Ori is already anomalous in the sense that it likely accelerates slowly. Theoretical calculations (e.g., Castor et al. 1975) predict β -values lower than unity. The question then is that if a star has a slowly accelerating wind ($\beta \sim 2$) and if the clumping scales with the wind velocity, why would the prescribed F_{cl} at V_{∞} be reached rapidly? Nevertheless, we are not in the position to decide which distribution is more

realistic, therefore we consider all the models with $F_{\text{cl}}= 0.05$, $F_{\text{cl}}= 0.3$, and $F_{\text{cl}}= 0.6$ as best-fitting models. However, we note that if our finding of a higher mass-loss rate is correct, it indirectly supports the idea that the UV resonance lines are strongly affected by vorosity.

Finally, we would like to comment on the evolutionary status of ϵ Ori. A pleasant side-effect of using actual evolutionary calculations to create stellar atmosphere models is that the result comes with immediate information on the evolutionary status of the subject star. As shown in the H-R diagrams of Figs. 3–5 as well as in Table 3, the locations of the best-fitting models are near the terminal age main sequence (TAMS) of the evolutionary track for $M_{\text{ini}} \sim 40M_{\odot}$. Furthermore, Table 3 shows that all the best-fitting models are from the batch that was calculated without considering the rotational enhancement in the surface abundances, which indirectly suggest that the star rotates slowly. This is consistent with the fact ϵ Ori has low $v \sin i$.

6. Summary

We presented a mega grid of 43,340 stellar atmospheric models calculated by the CMFGEN package, which will soon be ex-

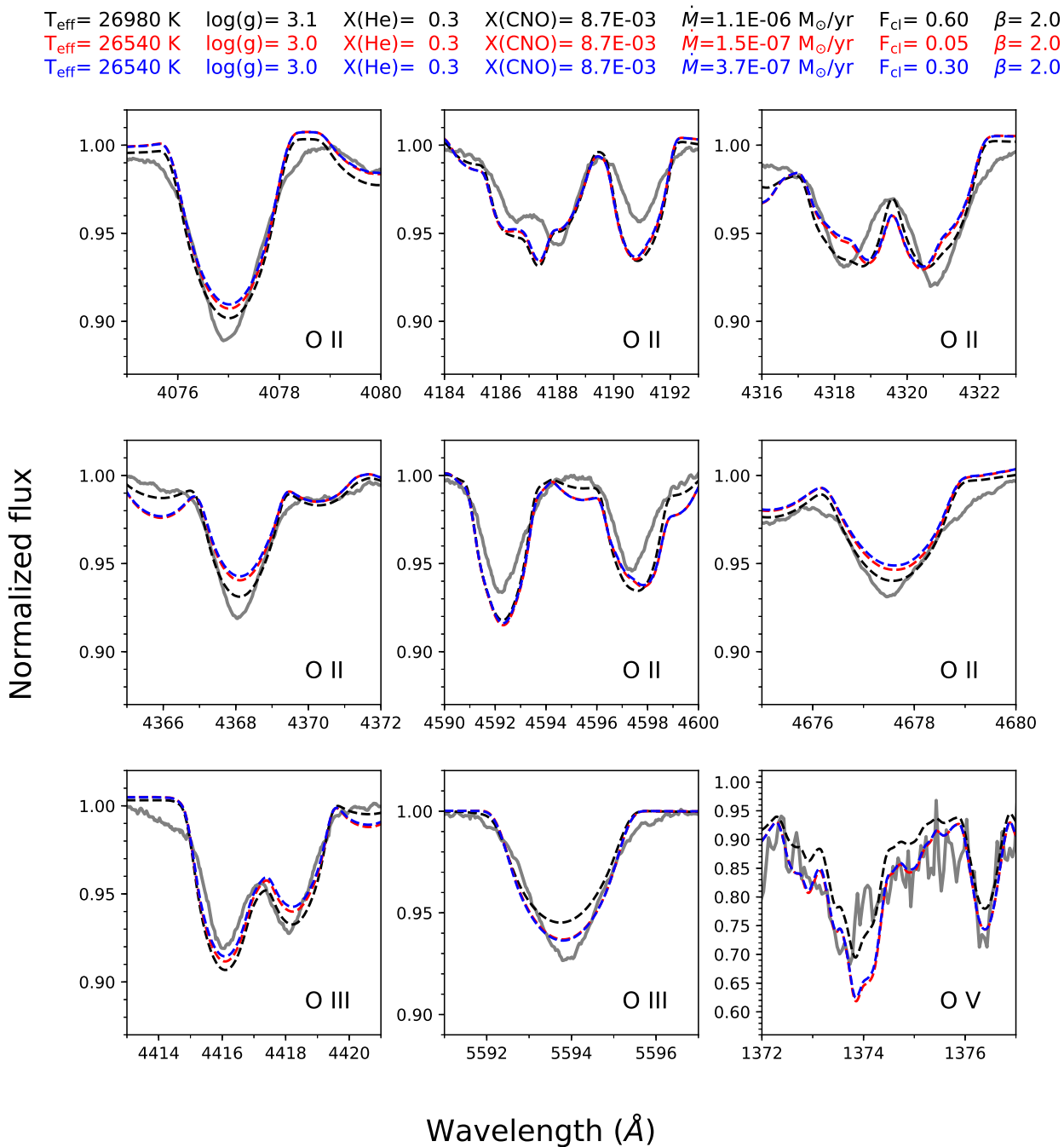


Fig. 12. Same as Fig. 8, but the comparison is for selected O lines.

tended to 80,000 models. These models cover the region of the H–R diagram that is populated by OB main-sequence and W-R stars with masses between 9 and $120 M_{\odot}$. The grid provides UV, visual, and IR spectra for each model.

We used the surface temperature (T_{eff}) and luminosity (L) values that correspond to the evolutionary traces and isochrones of Ekström et al. (2012). Furthermore, we used seven values of β , four values of the clumping factor, and two different metallicities and terminal velocities. This generated a six-dimensional hypercube of stellar atmospheric models that we intend to release to the general astronomical community as a free tool for analyzing the spectra of massive stars.

We have also demonstrated the usefulness of our mega-grid by reanalyzing ϵ Ori. Our somewhat crude but very rapid analysis supported the stellar and wind parameters reported by Puebla et al. (2016). The only significant difference is that our reanalysis favors the high end of the acceptable mass-loss range ($\dot{M} \sim 1.1 \times 10^{-6} M_{\odot} \text{ yr}^{-1}$) with a lower level of clumping. This result indirectly supports recent simulations that suggest that the UV resonance lines are highly affected by velocity-space porosity. The reason for the slightly different conclusion of our reanalysis is that we used a generic radial distribution of clumping, while Puebla et al. (2016) customized the distribution to ϵ Ori. It is not clear that our distribution is worse.

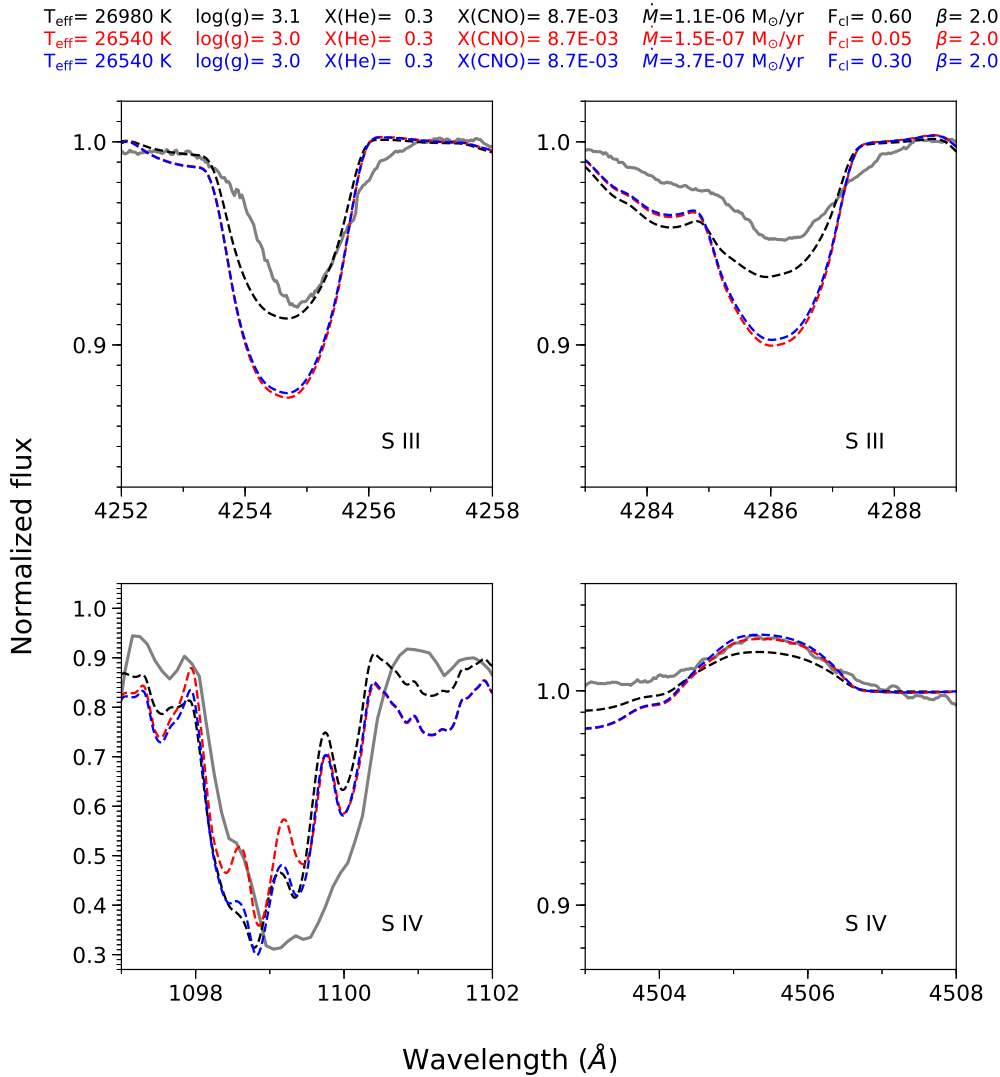


Fig. 13. Same as Fig. 8, but the comparison is for selected S lines.

The reanalysis showed the benefits of having a large grid of precalculated models. The stellar and wind parameters for a star can be calculated rapidly. If required, a more detailed study can then be performed, but by starting with good initial values. This significantly shortens the time that is needed to complete a spectral analysis.

Acknowledgements. All models and their synthetic spectra were calculated by the cluster Abacus I. The authors express their acknowledgement for the resources, expertise and the assistance provided by "ABACUS" Laboratory of Applied Mathematics and High Performance Computing CINVESTAV-IPN, CONACyT-EDOMEX-2011-C01-165873 Project. The authors are also grateful to D.J. Hillier, the author of the code CMFGEN, for his helpful comments during the production of the grid and during the preparation of this article. J. Zsargó acknowledges CONACyT CB-2011-01 No. 168632 grant for support. J. Klapp acknowledges financial support by the Consejo Nacional de Ciencia y Tecnología (CONACyT) of México under grant 283151. The authors also acknowledge the anonymous referee for his or her helpful comments and suggestions.

References

Asplund, M., Grevesse, N., Sauval, A. J., & Scott, P. 2009, *ARA&A*, 47, 481
 Bouret, J.-C., Lanz, T., Hillier, D. J., et al. 2003, *ApJ*, 595, 1182
 Carneiro, L. P., Puls, J., Sundqvist, J. O., & Hoffmann, T. L. 2016, *A&A*, 590, A88

Cassinelli, J. P., Miller, N. A., Waldron, W. L., MacFarlane, J. J., & Cohen, D. H. 2001, *ApJ*, 554, L55
 Castor, J., Abbott, D. C., & Klein, R. I. 1975, *ApJ*, 195, 157
 Cohen, D. H., Leutenegger, M. A., Grizzard, K. T., et al. 2006, *MNRAS*, 368, 1905
 Cohen, D. H., Leutenegger, M. A., Wollman, E. E., et al. 2010, *MNRAS*, 405, 2391
 Cohen, D. H., Wollman, E. E., Leutenegger, M. A., et al. 2014, *Monthly Notices of the Royal Astronomical Society*, 439, 908
 Crowther, P. A., Hillier, D. J., Evans, C. J., et al. 2002, *ApJ*, 579, 774
 Crowther, P. A., Lennon, D. J., & Walborn, N. R. 2006, *A&A*, 446, 279
 Ekström, S., Georgy, C., Eggenberger, P., et al. 2012, *A&A*, 537, A146
 Fierro, C. R., Borissova, J., Zsargó, J., et al. 2015, *PASP*, 127, 428
 Fierro-Santillán, C. R., Zsargó, J., Klapp, J., et al. 2018, *ApJS*, 236, 38
 Fullerton, A. W., Crowther, P. A., De Marco, O., et al. 2000, *ApJ*, 538, L43
 Gagné, M., Oksala, M. E., Cohen, D. H., et al. 2005, *ApJ*, 628, 986
 Gräfener, G. & Hamann, W.-R. 2008, *A&A*, 482, 945
 Gräfener, G., Koesterke, L., & Hamann, W.-R. 2002, *A&A*, 387, 244
 Hainich, R., Ramachandran, V., Shenar, T., et al. 2019, *A&A*, 621, A85
 Hamann, W.-R. & Gräfener, G. 2004, *A&A*, 427, 697
 Hauschildt, P. H. 1992, *J. Quant. Spectr. Rad. Transf.*, 47, 433
 Herald, J. E. & Bianchi, L. 2004, *PASP*, 116, 391
 Hillier, D. J. 2013, <http://kookaburra.phyast.pitt.edu/hillier/web/CMFGEN.htm>
 Hillier, D. J., Bouret, J.-C., Lanz, T., & Busche, J. R. 2012, *MNRAS*, 426, 1043
 Hillier, D. J., Lanz, T., Heap, S. R., et al. 2003, *ApJ*, 588, 1039
 Hillier, D. J. & Miller, D. L. 1998, *ApJ*, 496, 407
 Hillier, D. J. & Miller, D. L. 1999, *ApJ*, 519, 354
 Hubeny, I. & Lanz, T. 1995, *ApJ*, 439, 875

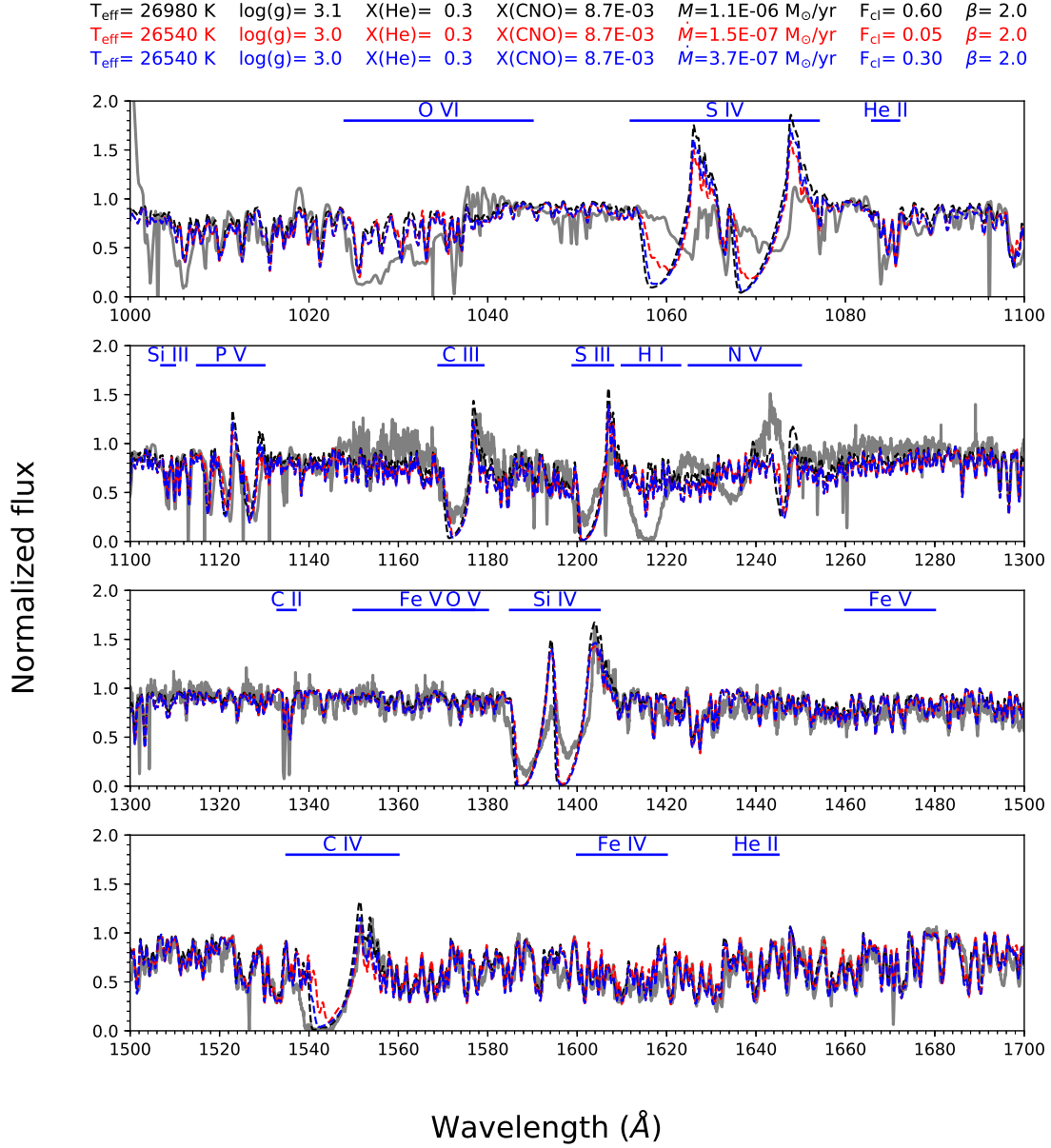


Fig. 14. Comparison of our best-fitting models (dashed black, red, and blue lines) with the UV spectra observed for ϵ Ori (solid gray line). The relevant model parameters are color-coded above the panels, and important UV lines marked above the spectra.

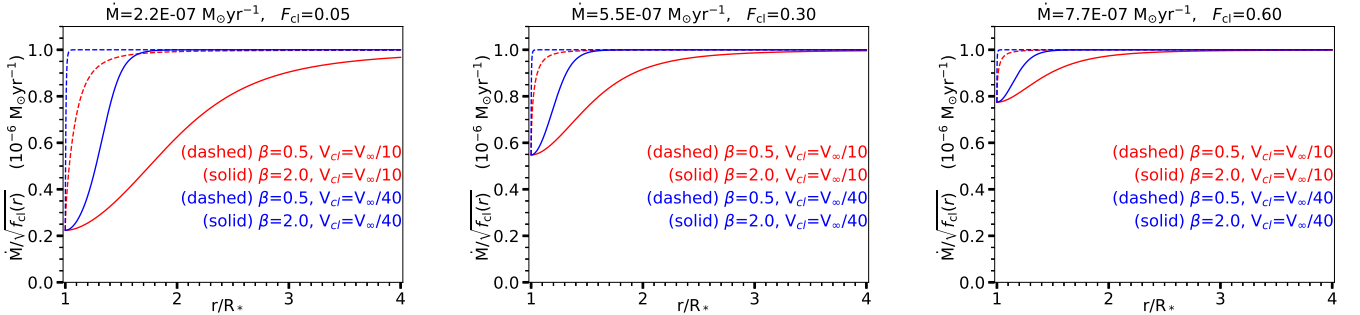


Fig. 15. True value of the ratio $\dot{M} / \sqrt{f_{\text{cl}}(r)}$ as a function of r/R_* for a typical O type star (relevant parameters are color-coded and listed above and in the body of each panel). This ratio controls the wind emission due to recombination of ionized hydrogen, i.e., the higher its value, the greater the emission. We used Eq. (2) with the different values of V_{cl} (color-coded in the body of each figure) to calculate f_{cl} .

- Kahn, S. M., Leutenegger, M. A., Cottam, J., et al. 2001, A&A, 365, L312
Kudritzki, R. P., Puls, J., Lennon, D. J., et al. 1999, A&A, 350, 970
Maeder, A. 1999, A&A, 347, 185
Maeder, A. & Meynet, G. 2000, A&A, 361, 159
Martins, F., Schaerer, D., & Hillier, D. J. 2002, A&A, 382, 999
Oskinova, L. M., Feldmeier, A., & Hamann, W. R. 2004, A&A, 422, 675
Owocki, S. P. & Cohen, D. H. 2006, ApJ, 648, 565
Palacios, A., Gebran, M., Josselin, E., et al. 2010, A&A, 516, A13
Pauldrach, A. W. A., Hoffmann, T. L., & Lennon, M. 2001, A&A, 375, 161
Puebla, R. E., Hillier, D. J., Zsargó, J., Cohen, D. H., & Leutenegger, M. A. 2016, MNRAS, 456, 2907
Puls, J., Urbaneja, M. A., Venero, R., et al. 2005, A&A, 435, 669
Rivero González, J. G., Puls, J., & Najarro, F. 2011, A&A, 536, A58
Runacres, M. C. & Owocki, S. P. 2002, A&A, 381, 1015
Sander, A., Shenar, T., Hainich, R., et al. 2015, A&A, 577, A13
Santolaya-Rey, A. E., Puls, J., & Herrero, A. 1997, A&A, 323, 488
Searle, S. C., Prinja, R. K., Massa, D., & Ryans, R. 2008, A&A, 481, 777
Sundqvist, J. O., Owocki, S. P., Cohen, D. H., Leutenegger, M. A., & Townsend, R. H. D. 2012, MNRAS, 420, 1553
Sundqvist, J. O. & Puls, J. 2018, A&A, 619, A59
Sundqvist, J. O., Puls, J., & Owocki, S. P. 2014, A&A, 568, A59
Vink, J. S., de Koter, A., & Lamers, H. J. G. L. M. 2001, A&A, 369, 574
Zsargó, J., Arrieta, A., Fierro, C., et al. 2017, in Astronomical Society of the Pacific Conference Series, Vol. 508, The B[e] Phenomenon: Forty Years of Studies, ed. A. Miroshnichenko, S. Zharikov, D. Korčáková, & M. Wolf, 407
Zsargó, J., Hillier, D. J., Bouret, J.-C., et al. 2008, ApJ, 685, L149

Appendix A:

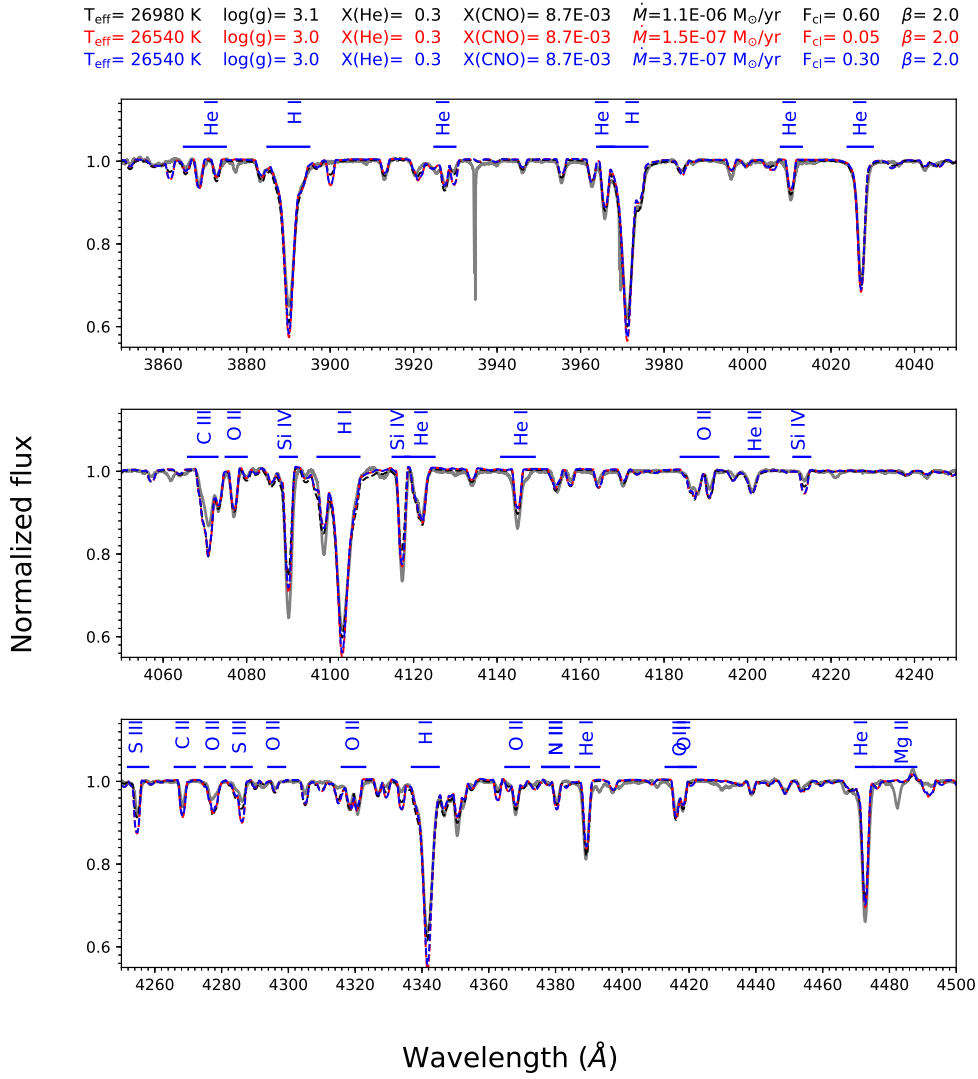


Fig. A.1. Comparison of our best-fitting models (dashed black, red, and blue lines) with the blue part of the optical spectra for ϵ Ori (solid gray line). The relevant parameters are color-coded and listed above the figure, and important lines are indicated above the spectra.

$T_{\text{eff}} = 26980 \text{ K}$ $\log(g) = 3.1$ $X(\text{He}) = 0.3$ $X(\text{CNO}) = 8.7\text{E-}03$ $\dot{M} = 1.1\text{E-}06 \text{ M}_{\odot}/\text{yr}$ $F_{\text{cl}} = 0.60$ $\beta = 2.0$
 $T_{\text{eff}} = 26540 \text{ K}$ $\log(g) = 3.0$ $X(\text{He}) = 0.3$ $X(\text{CNO}) = 8.7\text{E-}03$ $\dot{M} = 1.5\text{E-}07 \text{ M}_{\odot}/\text{yr}$ $F_{\text{cl}} = 0.05$ $\beta = 2.0$
 $T_{\text{eff}} = 26540 \text{ K}$ $\log(g) = 3.0$ $X(\text{He}) = 0.3$ $X(\text{CNO}) = 8.7\text{E-}03$ $\dot{M} = 3.7\text{E-}07 \text{ M}_{\odot}/\text{yr}$ $F_{\text{cl}} = 0.30$ $\beta = 2.0$

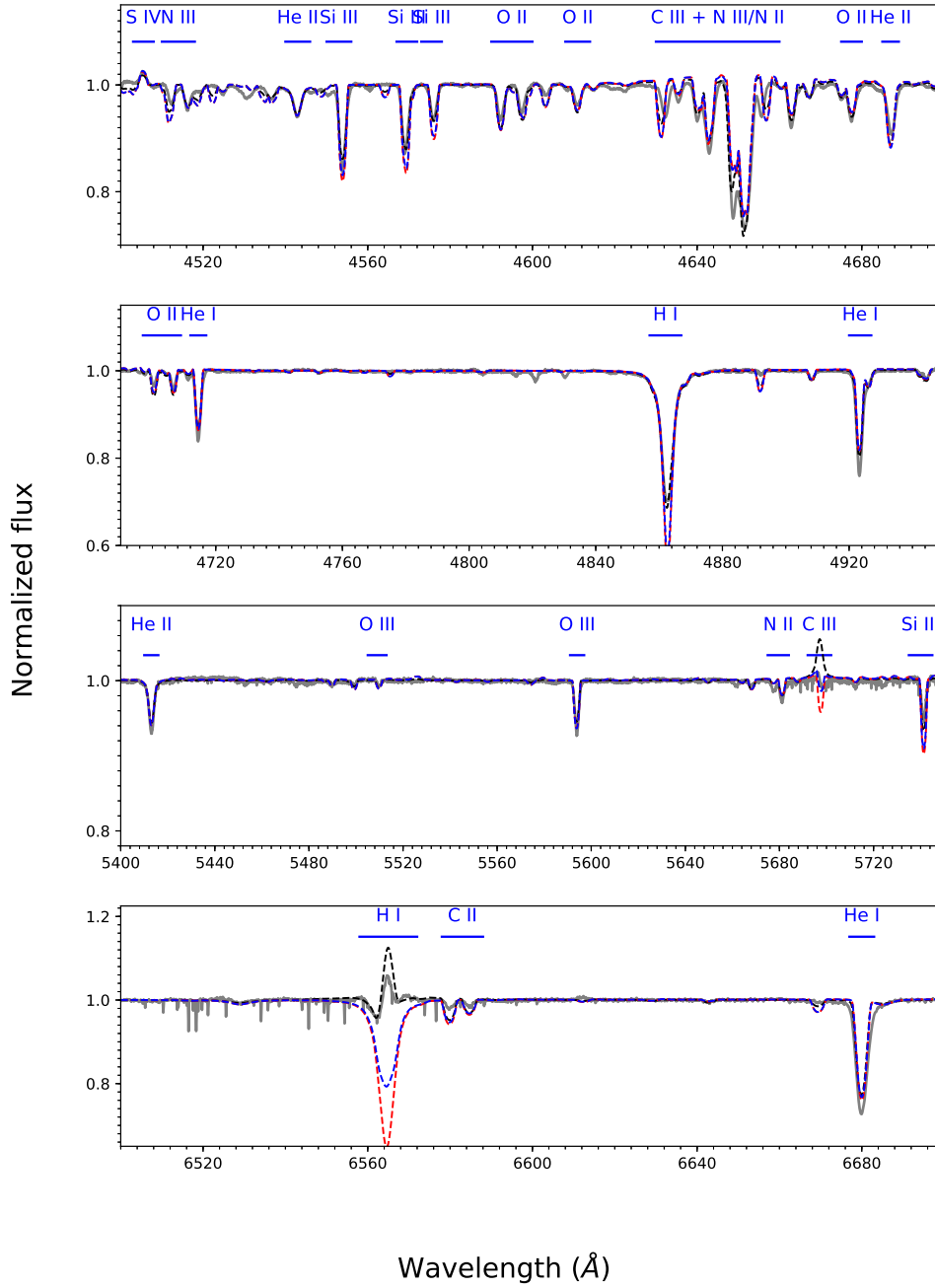


Fig. A.2. Same as Fig. A.1, but for the central region of the optical spectra.

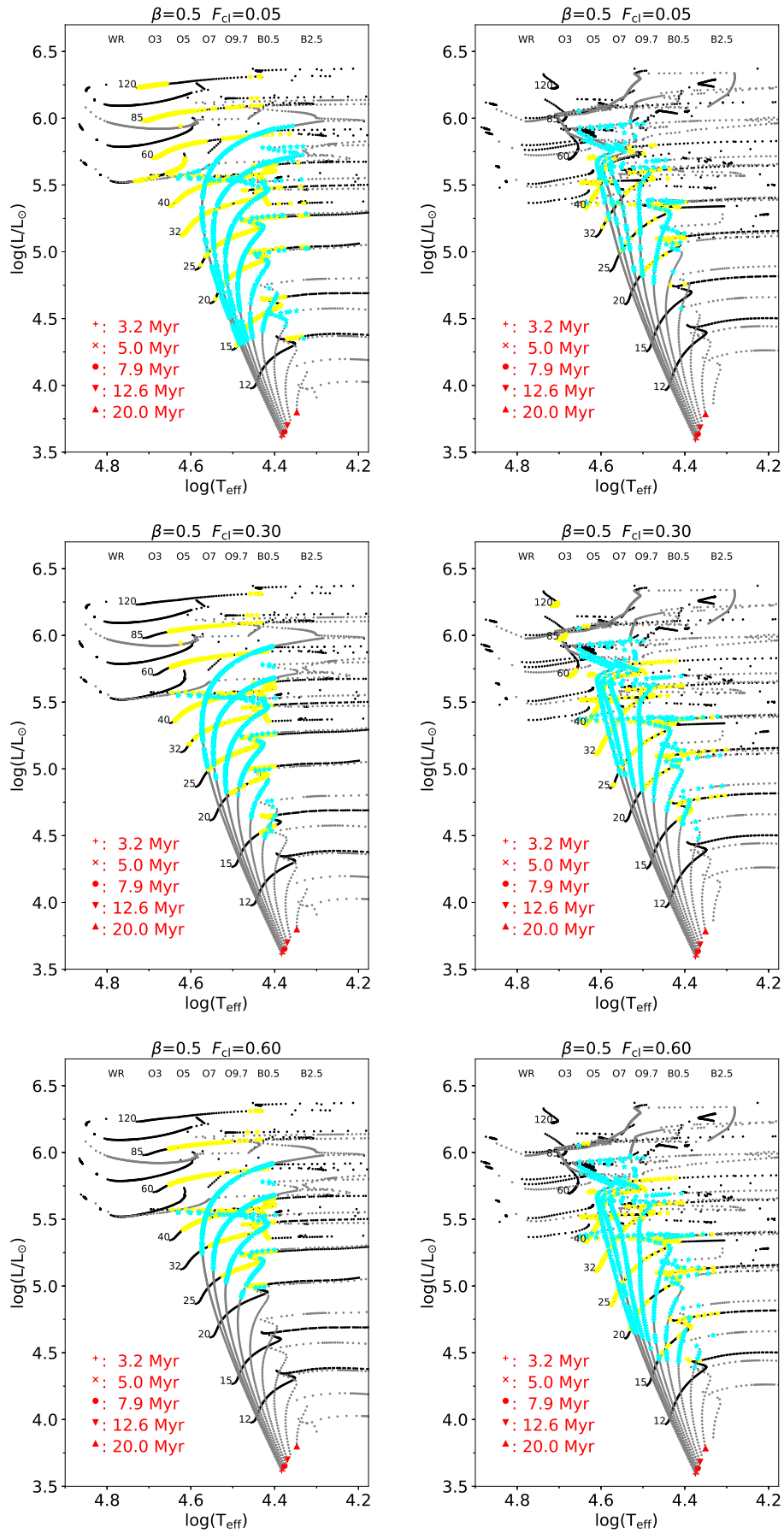


Fig. A.3. Sample of H-R diagrams, similar to Fig. 3, for various F_{cl} volume filling factors. The left and right columns show models without and with rotational enhancement, respectively.